Supplementary Information

Solvent-adaptive hydrogels with lamellar confinement cellular structure for programmable multimodal locomotion

Xin Yao[1], Hong Chen[1], Haili Qin[1], Qi-Hang Wu[1], Huai-Ping Cong[1]* & Shu-Hong Yu[2,3]*

[1] *Anhui Province Engineering Research Center of Flexible and Intelligent Materials, School of Chemistry and Chemical Engineering, Hefei University of Technology, Hefei 230009, P. R. China*

[2] *Institute of Innovative Materials, Department of Chemistry, College of Science, Southern University of Science and Technology, Shenzhen 518055, P. R. China*

[3] *New Cornerstone Science Laboratory, Division of Nanomaterials & Chemistry, Hefei National Research Center for Physical Sciences at the Microscale, Department of Chemistry, University of Science and Technology of China, Hefei 230026, P. R. China*

Correspondence should be addressed to the author: H. P. C. (hpcong@hfut.edu.cn) or S. H. Y. (yush@sustech.edu.cn).

This file includes:

Supplementary Methods

Supplementary Figures 1 to 46

Supplementary References 1 to 9

Other supplementary materials for this manuscript include the following:

Supplementary Movies 1 to 9

Supplementary Methods

Materials. Sodium alginate (SA) was purchased from Aladdin Chemistry Co., Ltd. N-isopropylacrylamide (NIPAM) was used as received from Tokyo Chemistry Industry Co., Ltd. N, N′-methylenebisacrylamide (MBAA, used as the chemical crosslinker) and potassium persulfate ($K_2S_2O_4$, used as the initiator) were purchased from National Pharmaceutical Group Chemical Reagent Co., Ltd. N,N,N′,N′-tetramethyl ethylenediamine (TEMED, used as the catalyst) was purchased from Bellway Technology Co. , Ltd. Carbon nanotubes (CNTs, 10-20 nm in diameter and 10-30 μm in length) were purchased from Nanjing XFNANO Materials Tech Co., Ltd and used as received. Other chemicals were purchased from National Pharmaceutical Group Chemical Reagent Co., Ltd.

Synthesis of AgNWs. The AgNWs were synthesized according to the reported protocol[1]. Typically, PVP (5.86 g) and glycerol (190 mL) were added into a 500 mL round bottle flask, followed with heating at 110 ℃ until dissolved completely. Ater cooling to room temperature, 1.58 g of $AgNO_3$ powder and NaCl solution (59 mg of NaCl dissolved in mixture containing 10 mL of glycerol and 0.5 mL of deionized water) were sequentially added into above solution with gently stirring. Then, the solution was heated at 210 ℃ for 30 min. When the solution color turned from pale white, light brown into gray-green, the AgNWs were prepared by centrifugating and washing for three times to remove the residual PVP.

Supplementary Note 1. The simulations of photothermal buoyancy flow induced by ASPC hydrogel. The thermo-induced fluid motion derived from the efficient photothermal conversion of the hydrogel under light stimulation. According to the heat balance equation in fluids interface, we obtained the following equation:

$$\rho C_p\left(\frac{\partial T}{\partial t}+\upsilon\cdot\nabla T\right)+\nabla\cdot(q+q_r)=\alpha_p T\left(\frac{dp}{dt}+\upsilon\cdot\nabla p\right)+\tau\colon\nabla\upsilon+Q \quad (1)$$

Where ρ was density of fluid, C_p was the specific heat capacity of fluid at constant pressure, v was the fluid velocity, T was the temperature of hydrogel, q was the heat flux by conduction, q_r was the heat flux by radiation, α_p was the coefficient of thermal expansion of fluid, p was the pressure, τ was the viscous stress tensor and Q was contained heat sources other than viscous dissipation. For a steady-state problem, the temperature does not change with time and terms with time derivatives disappear.

The first term of the right-hand side of equation (1) was the work done by pressure changes and was the result of heating under adiabatic compression as well as some thermoacoustic effects. It was generally small for low Mach number flows:

$$Q_P=\alpha_p T\left(\frac{dp}{dt}+\upsilon\cdot\nabla p\right) \quad (2)$$

And the heat flux was expressed by the following formula:

$$q=-k\frac{dT(x)}{dx} \quad (3)$$

Where the k was the thermal conductivity.

In addition, for low viscosity fluids, ignoring the viscous dissipation and Q could be ignored due to no heat was generated since the light absorption of fluid. The equation (1) could be simplified as

$$\rho C_p\upsilon\cdot\nabla T-\nabla\cdot(k\nabla T)=0 \quad (4)$$

Besides, for incompressible fluids, according to the Navier-Stokes equation describes this profile of fluid velocity:

$$\rho\left(\frac{d\upsilon}{dt}+(\upsilon\cdot\nabla)\upsilon\right)=-\nabla p+\mu\nabla^2\upsilon+f \quad (5)$$

Where μ was the fluid viscosity and f was the force generated by the temperature gradient.

Usually, in natural convection, f was the temperature-dependent buoyancy force, and could be estimated as:

$$f(T) = \alpha_p g(T - T_0) \tag{6}$$

Where α_p was the coefficient of thermal expansion of fluid, g was the gravitational acceleration, T_0 was the initial temperature of the fluid. So, the equation (5) could be expressed as

$$\rho\left(\frac{d\upsilon}{dt} + (\upsilon \cdot \nabla)\upsilon\right) = -\nabla p + \mu\nabla^2\upsilon + \alpha_p g(T - T_0) \tag{7}$$

We chose to solve numerically in parallel equations (4) and (7) using COMSOL Multiphysics. Based on the axisymmetric properties of the studied system, a two-dimensional model was created to solve the problem. The heat transfer (ht) and laminar flow (spf) modules were used to solve for transient values of coupled fields. The physical parameters of ethanol were taken from the COMSOL library. No slip boundaries were considered and set as thermal insulation. The length of the hydrogel was set at 3 mm and 1 mm from the lower boundary of the flow field. The shape of the flow field was set as a two-dimensional rectangle whose length and height were 30 mm and 10 mm, respectively. (T - T_0) was set to be 10 K, 20 K, 30 K, 40 K and 50 K, and T_0 was set to be 293K.

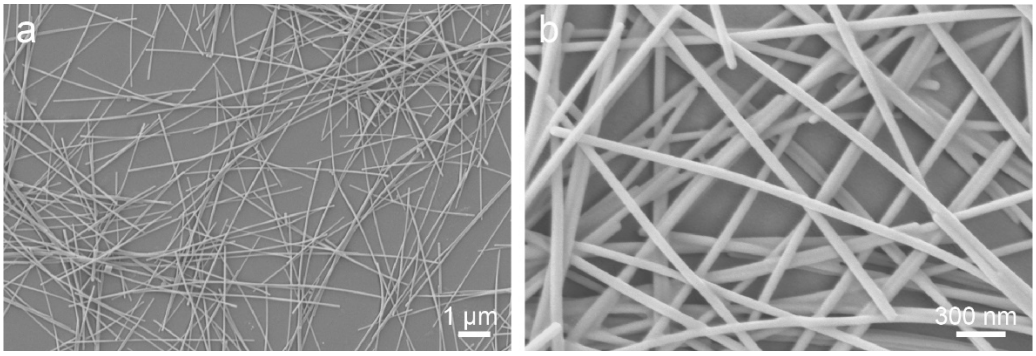

Supplementary Figure 1. SEM images with different magnifications of the AgNWs.

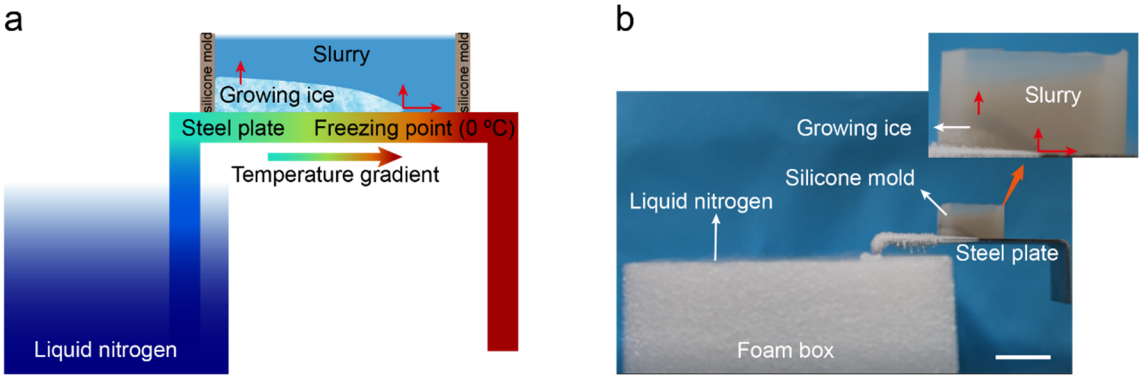

Supplementary Figure 2. Schematic illustrations (a) and optical images (b) of bidirectional freezing process. Scale bar: 1 cm. A home-made bidirectional freezing device was made of a foam box containing liquid nitrogen, a steel plate with high thermal conductivity and a silicone mold with adjustable shape. In the bidirectional freezing process, a steel plate was inserted to the foam box and a customized silicone mold was placed on the steel plate with 1 cm away from the cold source. After the slurry was added to the silicone mold, liquid nitrogen slowly poured into the foam box. The dual temperature gradients were therefore produced on the plate surface, which controlled the growth of ice crystals in the suspension in both horizontal and vertical directions. Ultimately, a parallel arranged ASAA layered structure was prepared under the effect of expelling the AgNWs and SA by the ice crystals.

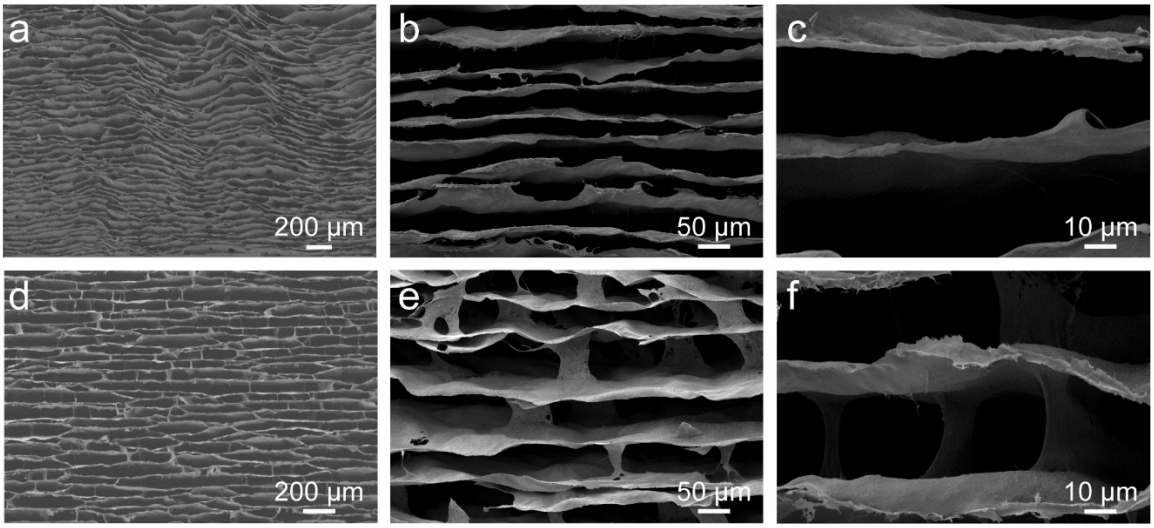

Supplementary Figure 3. SEM images with different magnifications of A_{10}SAA (a-c) and A_{45}SAA (d-f).

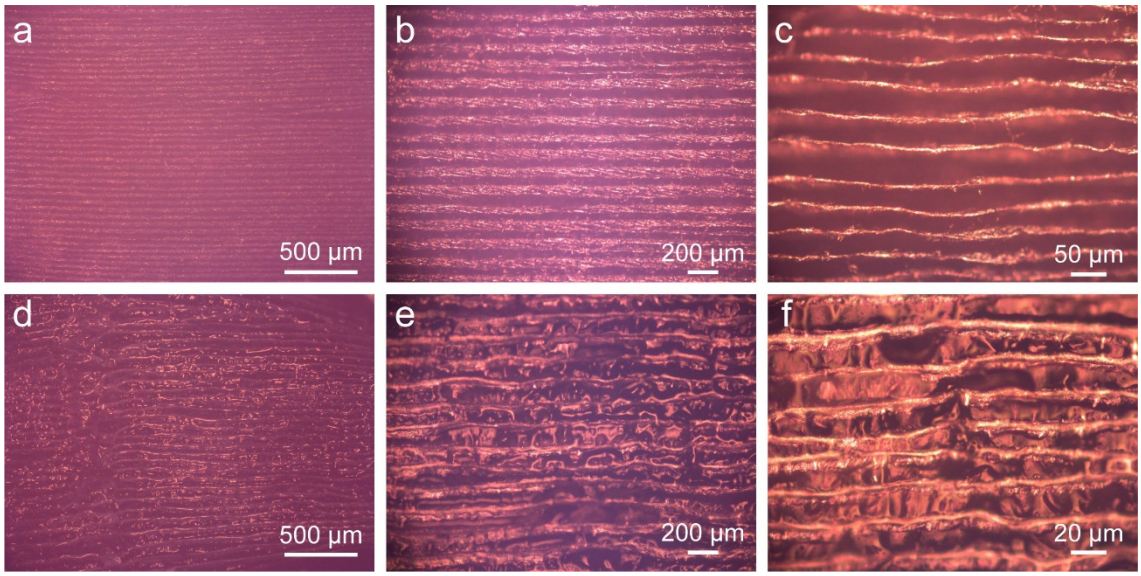

Supplementary Figure 4. Optical images with different magnifications of ASAA scaffold (a-c) and ASPC hydrogel (d-f).

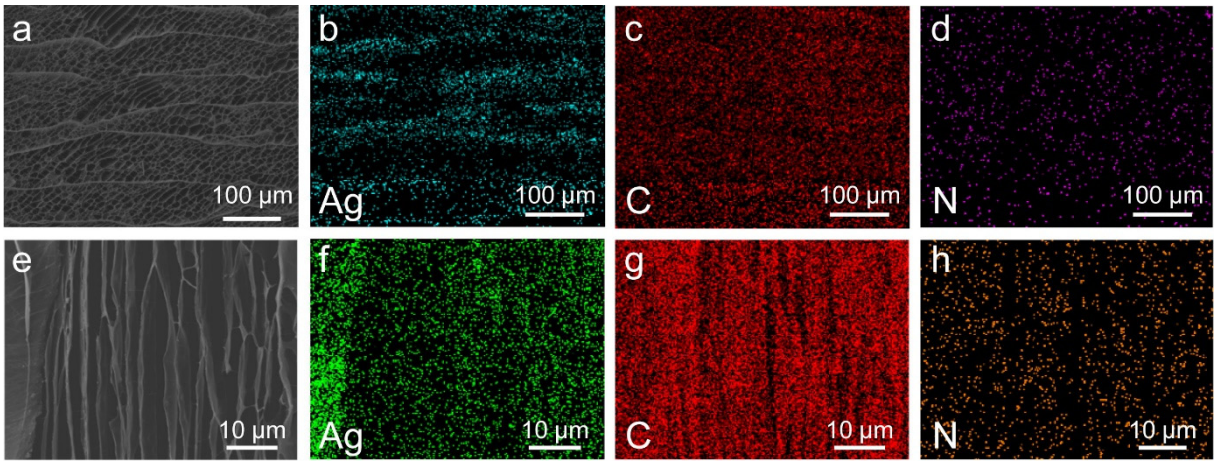

Supplementary Figure 5. SEM images and corresponding elemental mappings of the ASPC hydrogel: (a-d) top view; (e-h) side view.

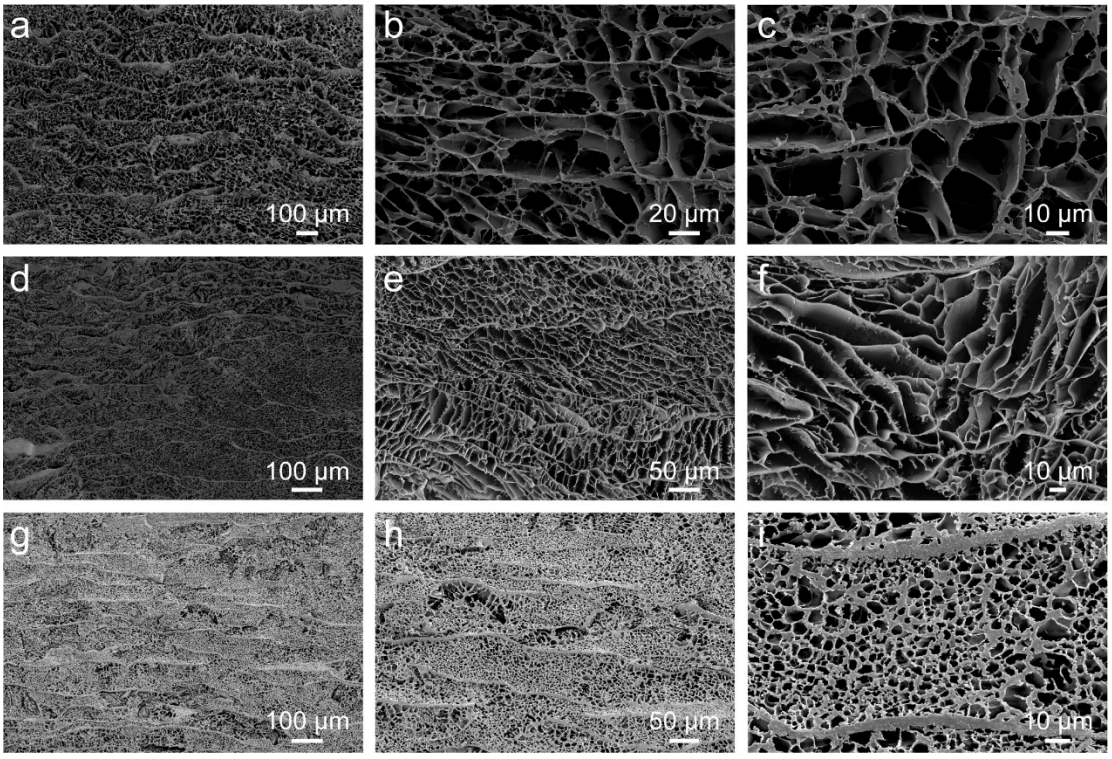

Supplementary Figure 6. Top-view SEM images with different magnifications of A_{10}SPC (a-c), A_{45}SPC (d-f) and ASAA-PC hydrogel (g-i).

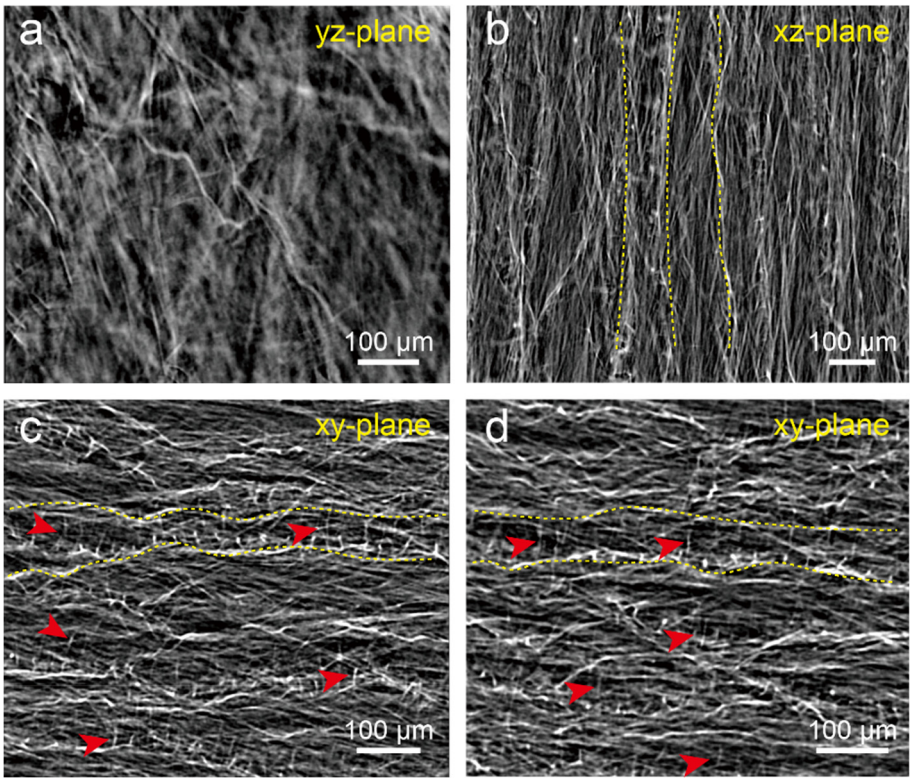

Supplementary Figure 7. Micro-CT images of different planes in the ASPC hydrogel. (a) *yz* plane: parallel to the AgNW/SA lamellae, (b) *xz* plane: perpendicular to the lamellae, and (c, d) *xy* plane: perpendicular to the lamellae. The yellow dashed lines and red arrows indicated the Ag/SA lamellae and nanopillars perpendicular to adjacent layers, respectively.

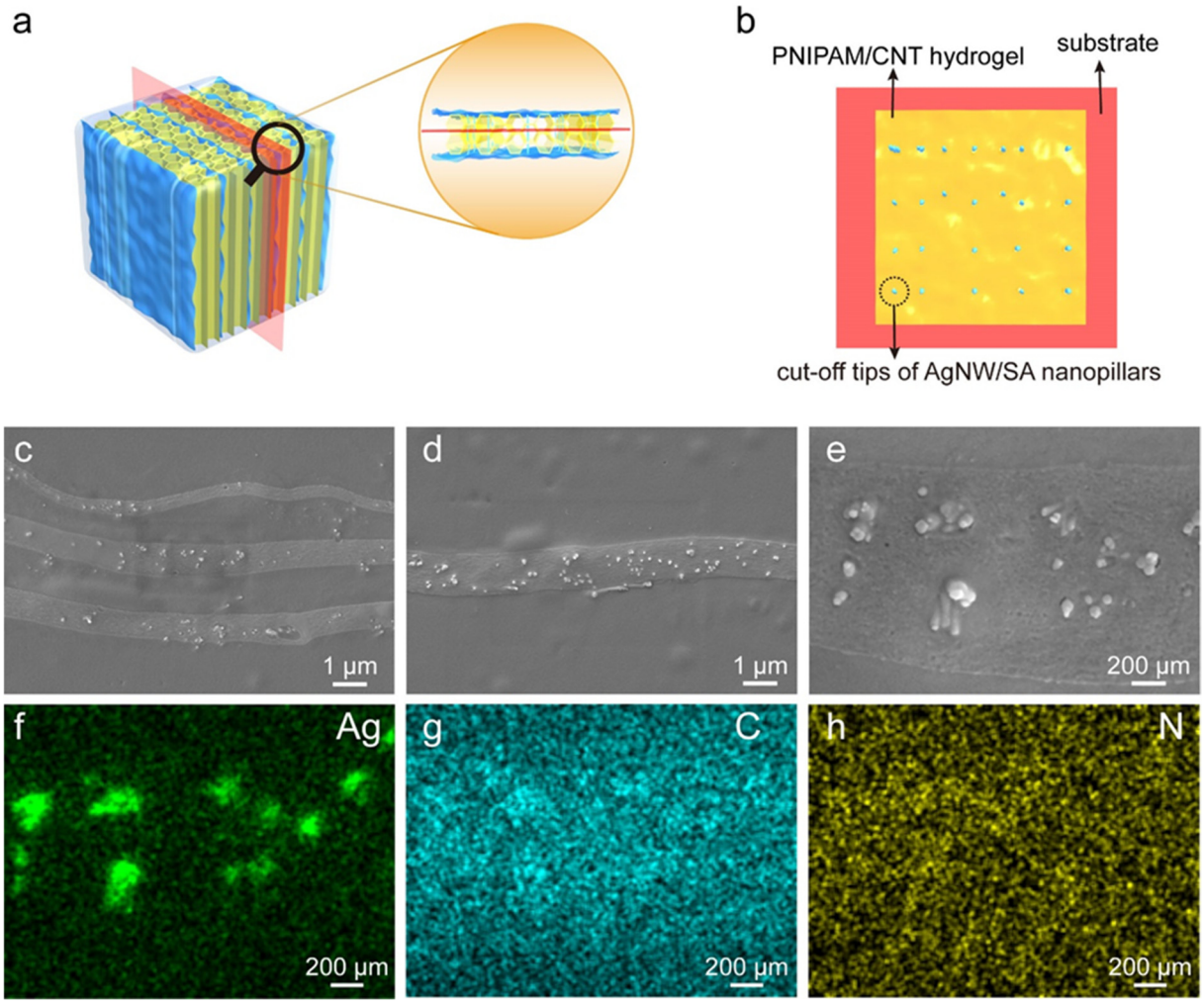

Supplementary Figure 8. Structural characterization of AgNW/SA nanopillars. (a) Schematic illustration showed the cutting of ultrathin slice parallel to the lamellae. (b) Schematic illustration of cut-off tips of AgNW/SA nanopillars. SEM images (c-e) and corresponding elemental mappings (f-h) of ultrathin slice of the ASPC hydrogel parallel to the lamellae.

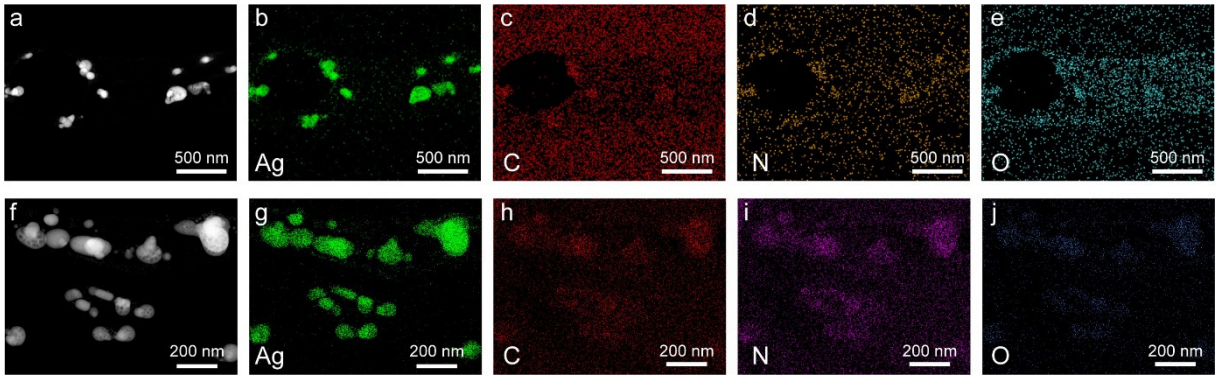

Supplementary Figure 9. HAADF-STEM images with different magnifications (a, f) and corresponding elemental mappings (b-e, and g-j) of ultrathin slice of the ASPC hydrogel parallel to the lamellae.

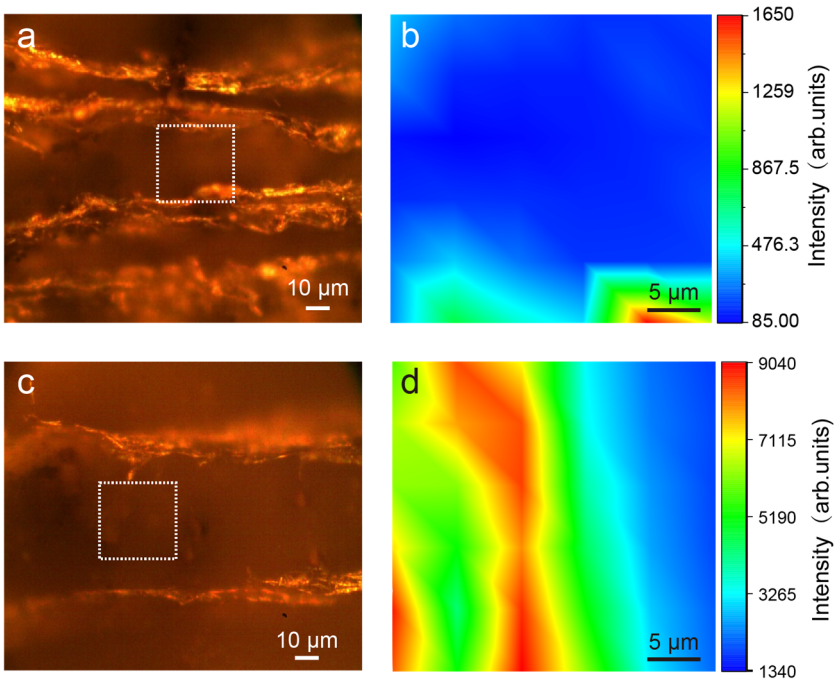

Supplementary Figure 10. Optical images showing lamellar structure of the A_{10}SPC (a) and A_{45}SPC hydrogel (c). (b, d) Raman scattering mapping of the region squared in (a) and (c).

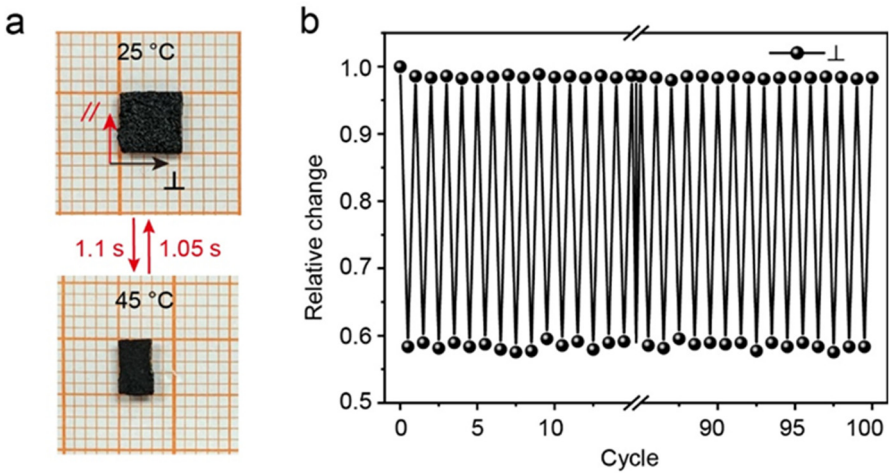

Supplementary Figure 11. Thermal-responsive anisotropic deformation of ASPC hydrogel. (a) Optical images of the hydrogel before and after heating. (b) The reversible deformation of ASPC hydrogel upon cyclically immersing into 25 ℃ and 45 ℃ water bath (100 cycles without obvious fatigue).

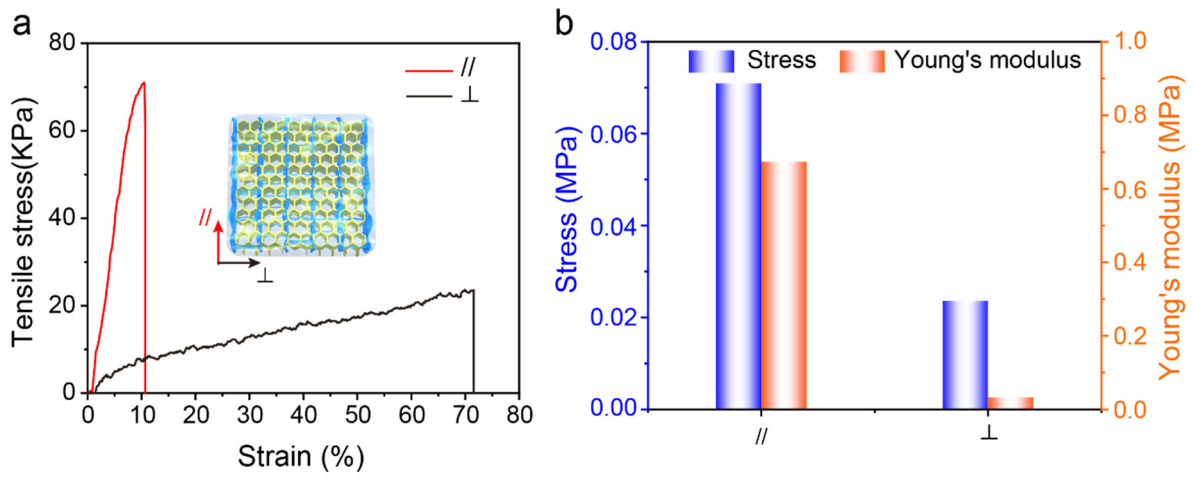

Supplementary Figure 12. Anisotropic mechanical behavior of ASPC hydrogel. (a) Tensile stress-strain curves stretched from the direction parallel (//) and perpendicular (⊥) to AgNW/SA lamellae. (b) The stress and Young's modulus calculated from the tensile stress-strain curves.

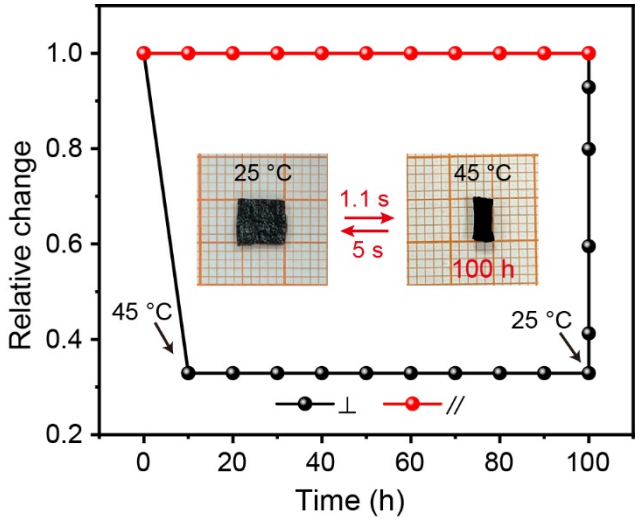

Supplementary Figure 13. Variations of the dimensions parallel and perpendicular to lamellae of ASPC hydrogel by immersing in 45 ℃ hot water for 100 h and then transferring in 25 ℃ water. It showed rapid recovery to its original shape in 5 s after cooling.

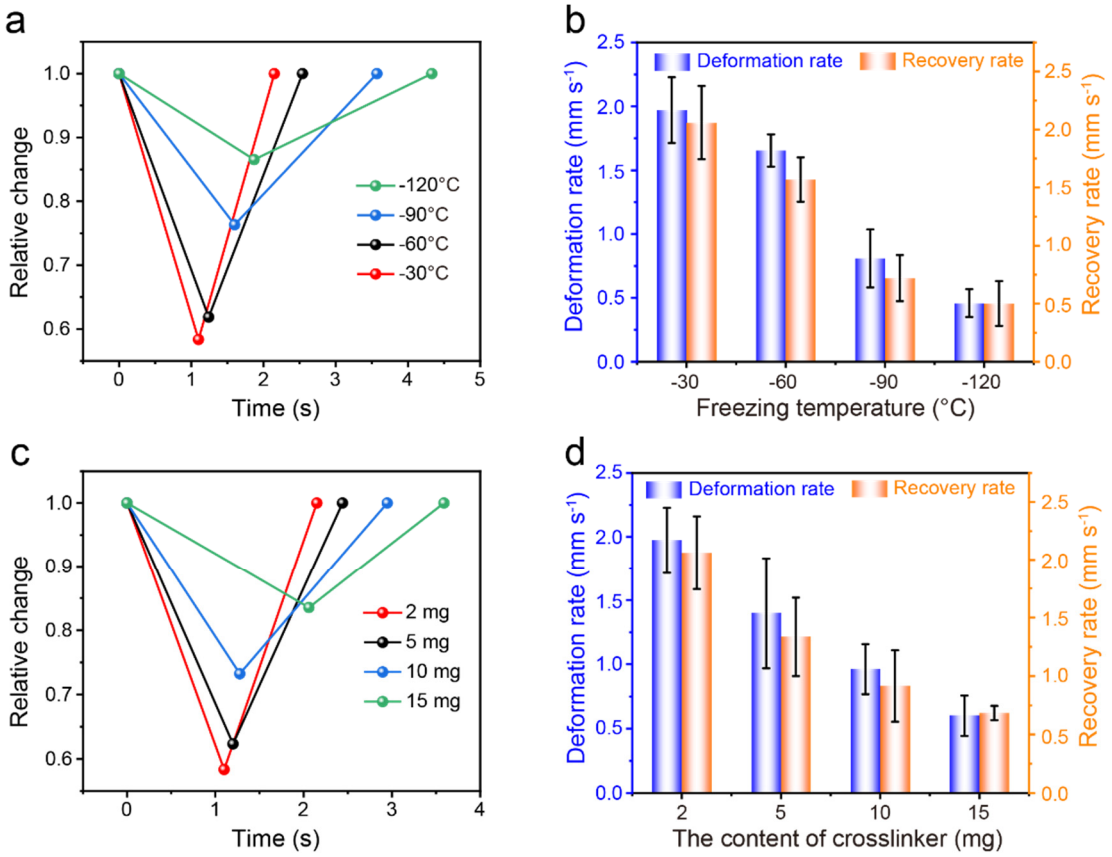

Supplementary Figures 14. Effects of unidirectional freezing temperature and crosslinker content on thermal-responsive performances of ASPC hydrogel. (a) Relative change of the size perpendicular to the lamellae and (b) deformation and recovery rates at different freezing temperatures. (c) Relative change of the size perpendicular to the lamellae and (d) deformation and recovery rates at different crosslinker contents. Data are presented as mean values ± SD (*n* = 3).

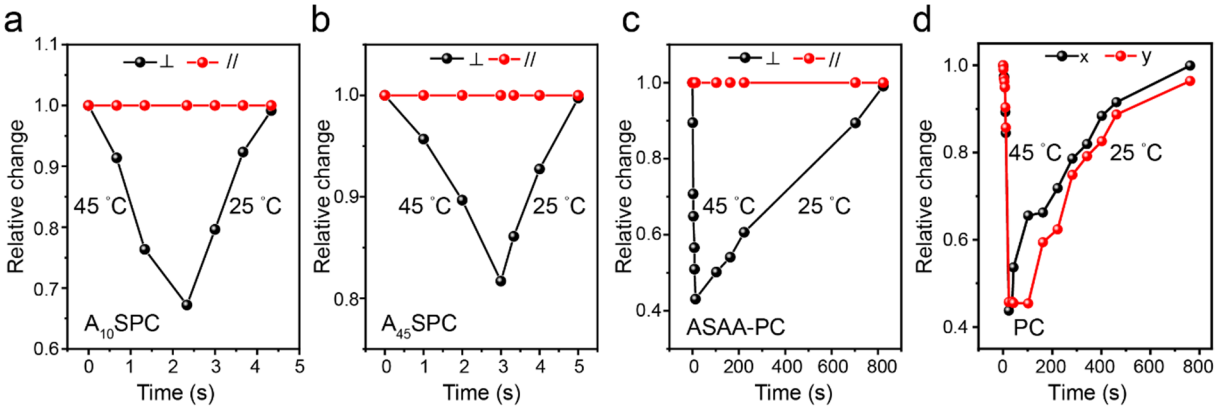

Supplementary Figure 15. Time-dependent relative changes of dimensions parallel and perpendicular to lamellae of four control hydrogels by immersing in 45 °C hot water and then transferring in 25 °C water. (a) A_{10}SPC, (b) A_{45}SPC, (c) ASAA-PC hydrogel and (d) PC hydrogel by in-situ polymerization of PNIPAM and CNTs.

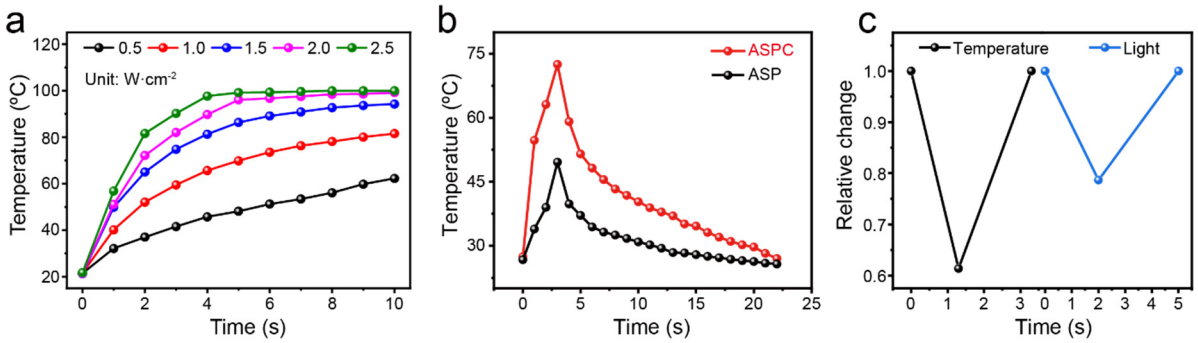

Supplementary Figure 16. (a) Variations of temperature of the ASPC hydrogel under the NIR irradiation at different laser intensities. The temperature of the hydrogel promptly increased from 22 ℃ to 40.2 ℃ within 1 s at an intensity of 1.0 W cm^{-2}. (b) Variations of temperature of ASPC hydrogel and ASP hydrogel without CNTs under irradiation. Power intensity: 1.5 W cm^{-2}. (c) Relative change of ASP hydrogel perpendicular to the lamellae under the stimuli of temperature and light.

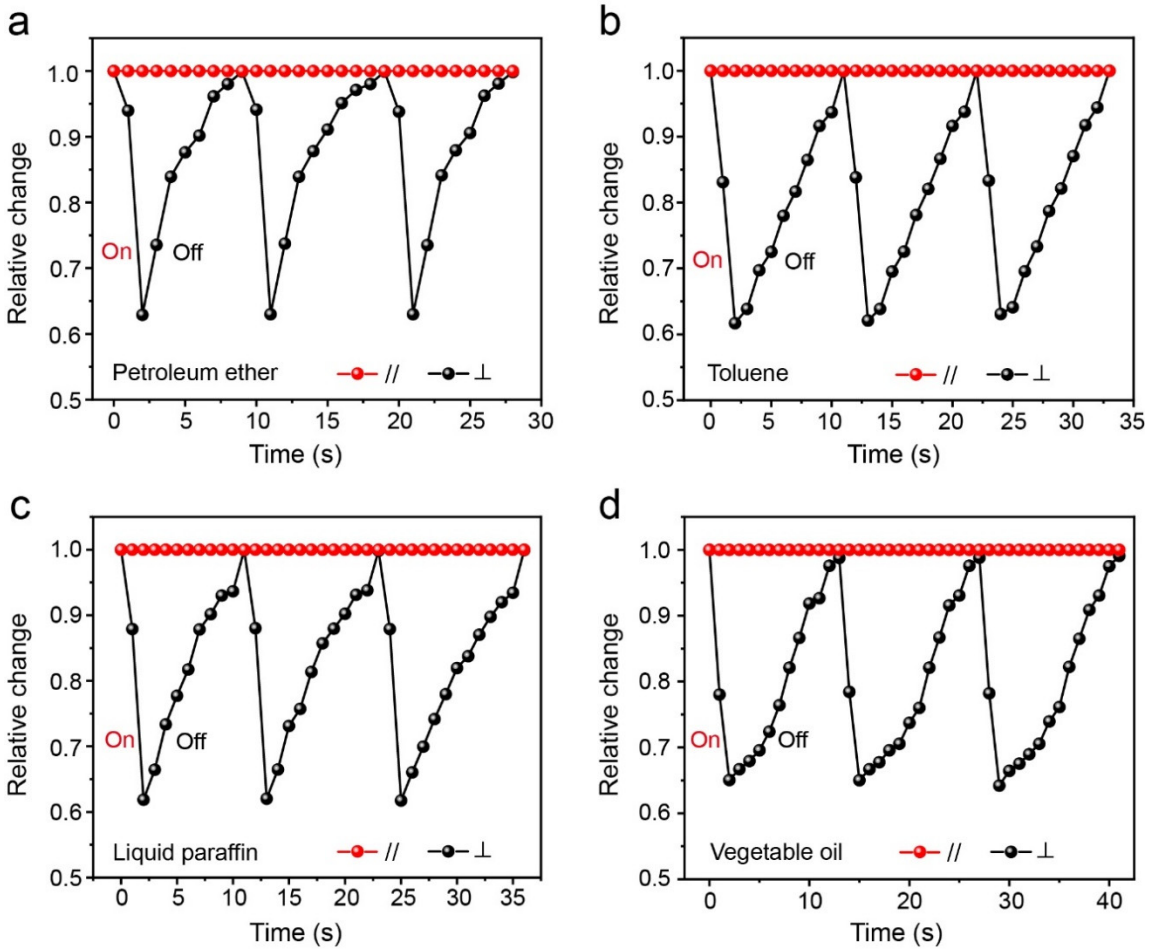

Supplementary Figure 17. Photoresponsive anisotropic deformation of ASPC hydrogel in different non-polar solvents: (a) petroleum ether, (b) toluene, (c) liquid paraffin and (d) vegetable oil.

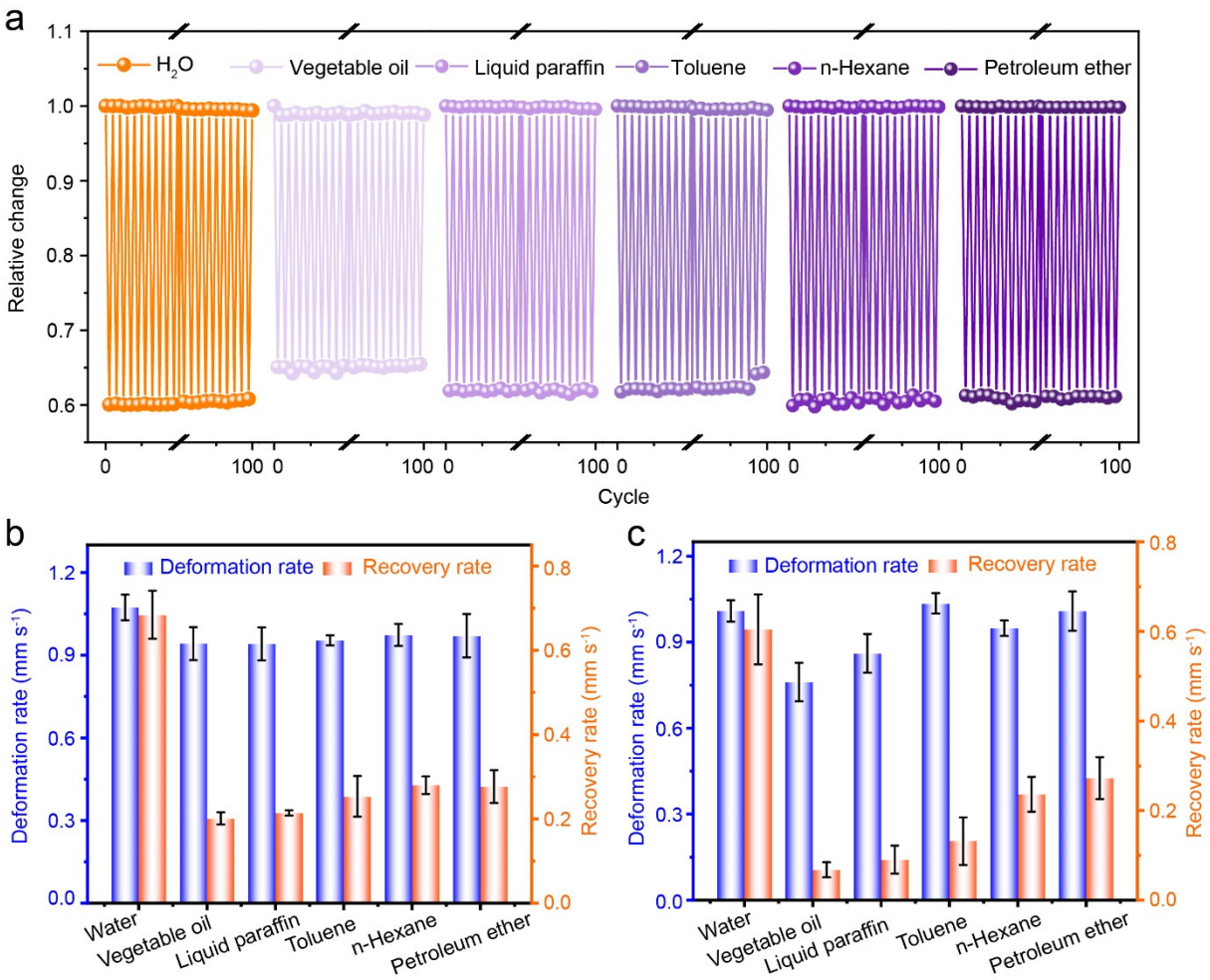

Supplementary Figure 18. (a) Relative changes of the dimension perpendicular to lamellae of the ASPC hydrogel in water, vegetable oil, liquid paraffin, toluene, *n*-hexane and petroleum ether over 100 cycles of on/off NIR irradiation. Summary of deformation and recovery rates of in different liquids under NIR stimulation before (b) and after 100 cycles (c). Data are presented as mean values ± SD (n = 3).

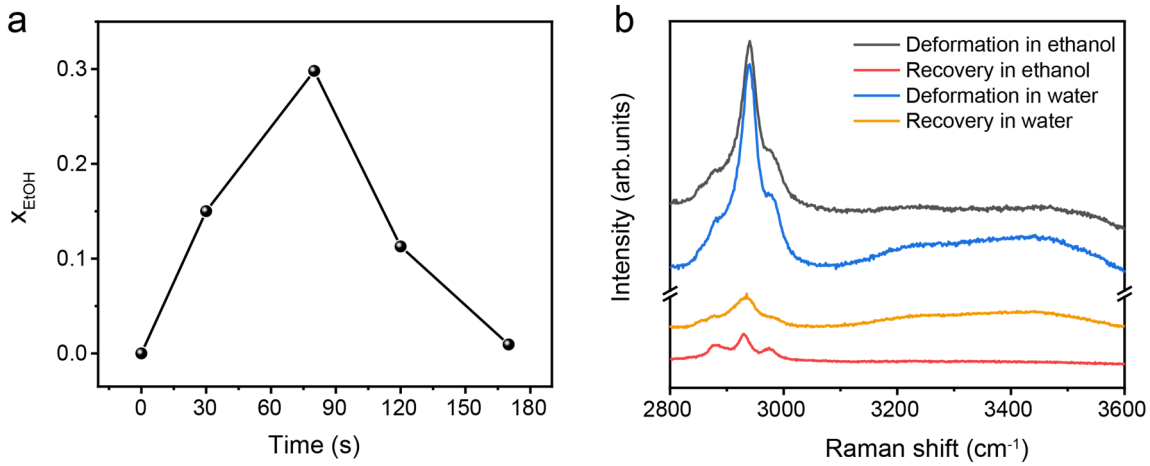

Supplementary Figure 19. Ethanol-stimulation mechanism of ASPC hydrogel. (a) The molar ratios of ethanol in hydrogel during the ethanol-stimulation process. (b) The υ(CH) bands in Raman spectra at different deformation stages. It was found that the intensity of the CH-stretching band located at 2800-3000 cm^{-1} changed periodically during the deformation and recovery processes.

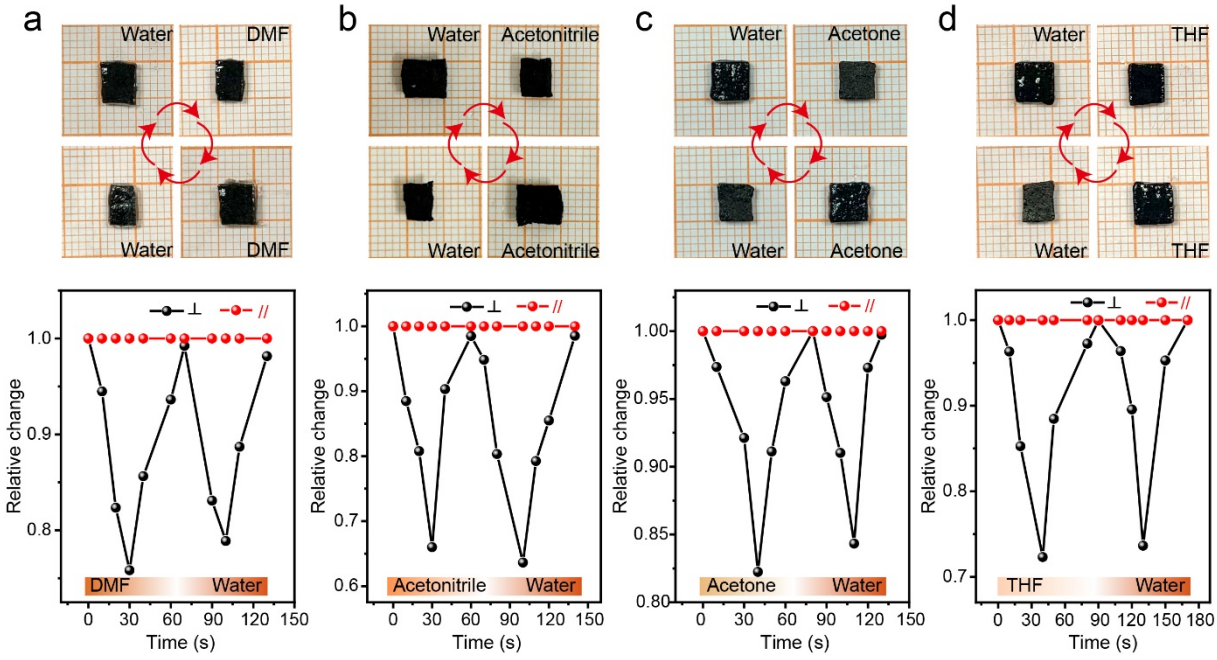

Supplementary Figure 20. Optical images (upper) and relative size changes (lower) showing stimuli-responsive deformations of ASPC hydrogels in DMF (a), acetonitrile (b), acetone (c), and THF (d).

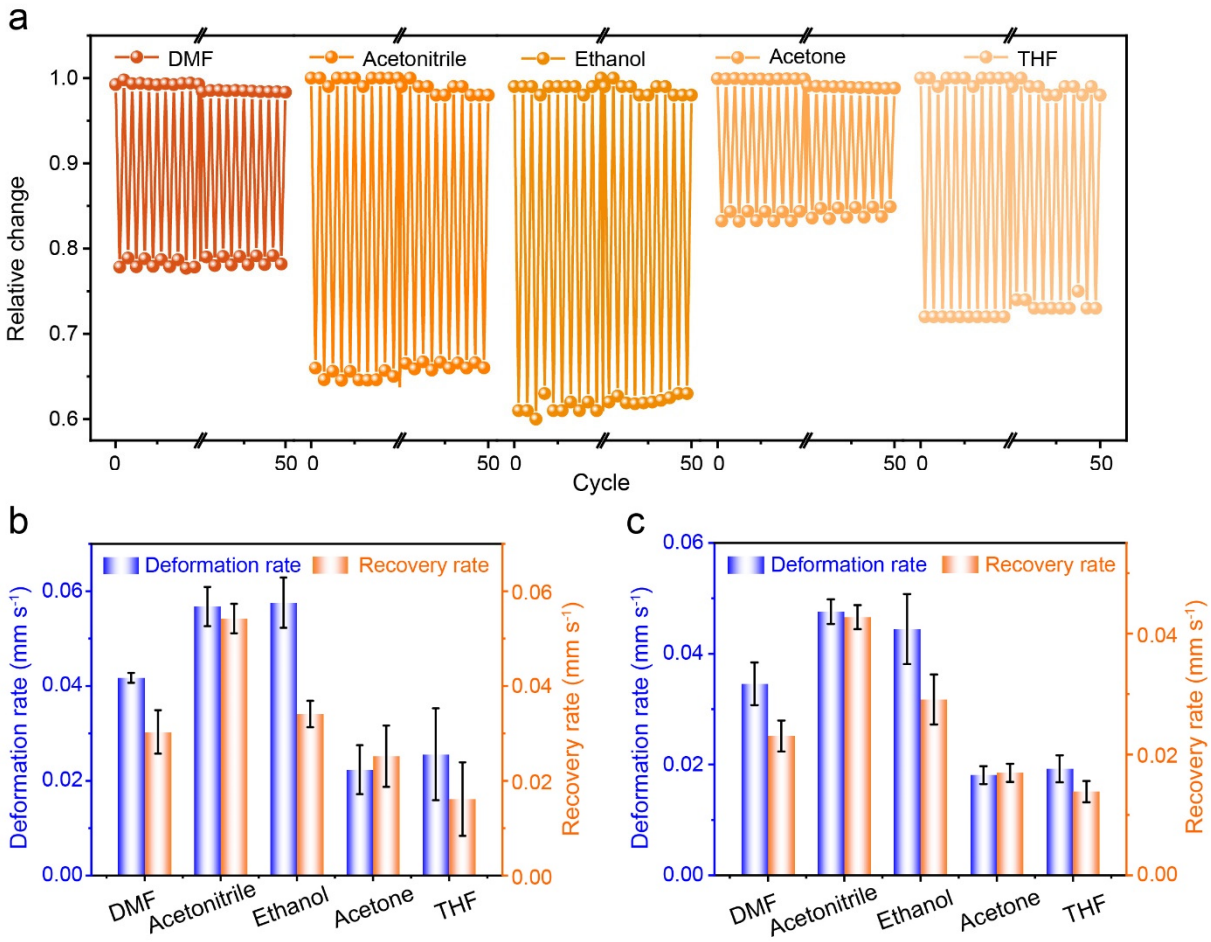

Supplementary Figure 21. (a) Cyclic stability of dimension variations of the ASPC hydrogel stimulated by DMF, acetonitrile, ethanol, acetone and THF. Summary of deformation and recovery rates of the ASPC hydrogel before (b) and after 50 cycles (c) of solvent stimulation. Data are presented as mean values ± SD (n = 3).

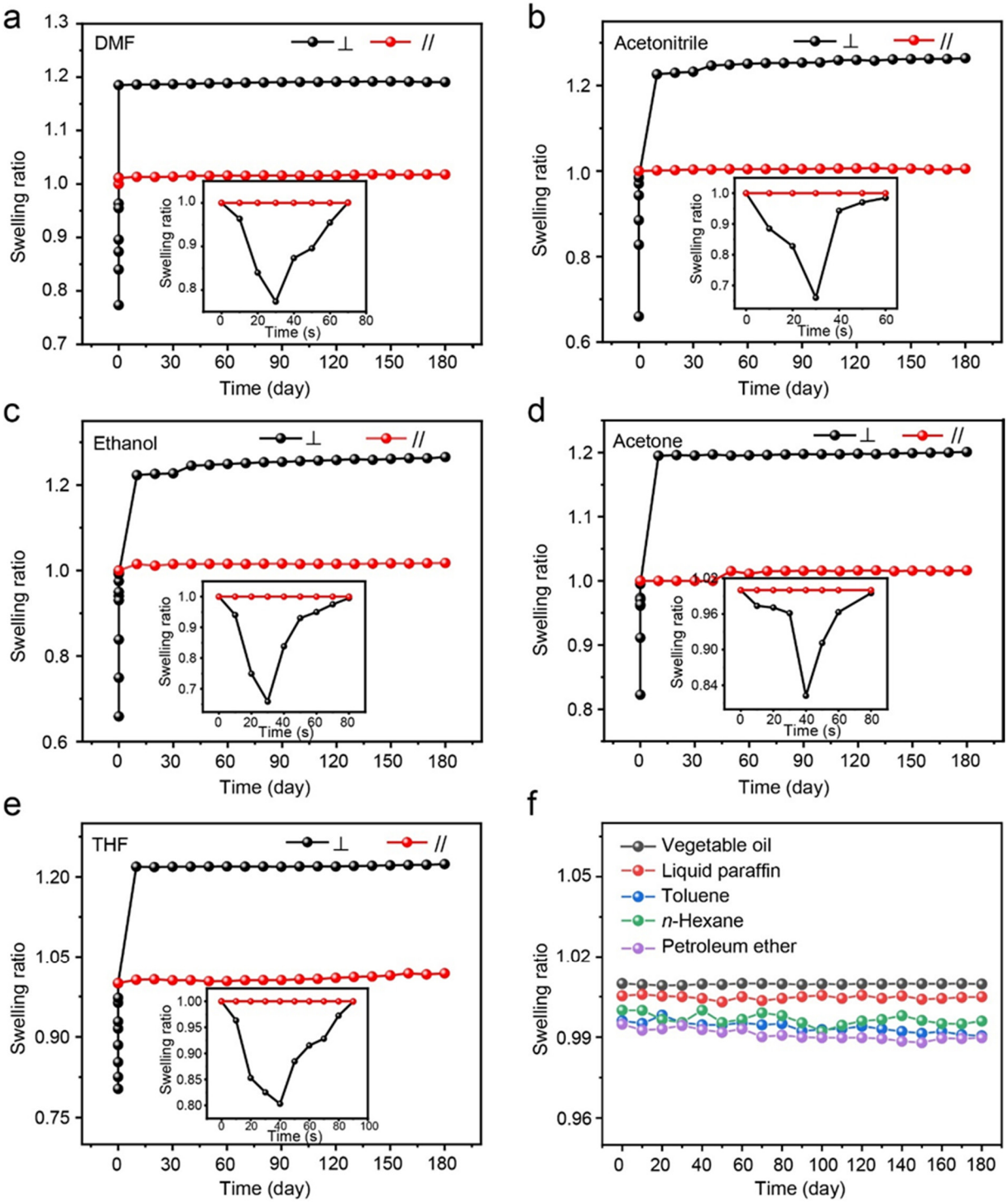

Supplementary Figure 22. Long-term stability of ASPC hydrogel in different solvents. Time-dependent swelling ratio of the dimensions parallel and perpendicular to lamellae of the ASPC hydrogel in polar solvents (a-e) and non-polar solvents (f) over 180 days.

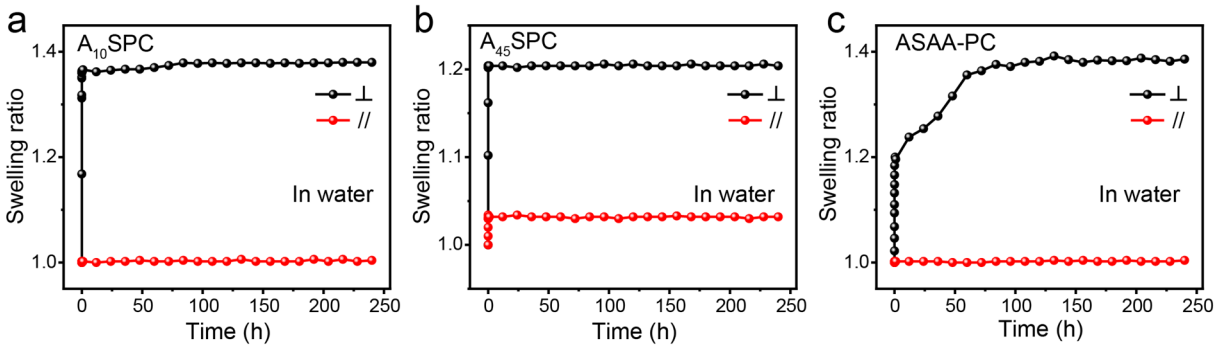

Supplementary Figure 23. Swelling behaviors of A_{10}SPC (a), A_{45}SPC (b) and ASAA-PC (c) hydrogels in water over 10 days.

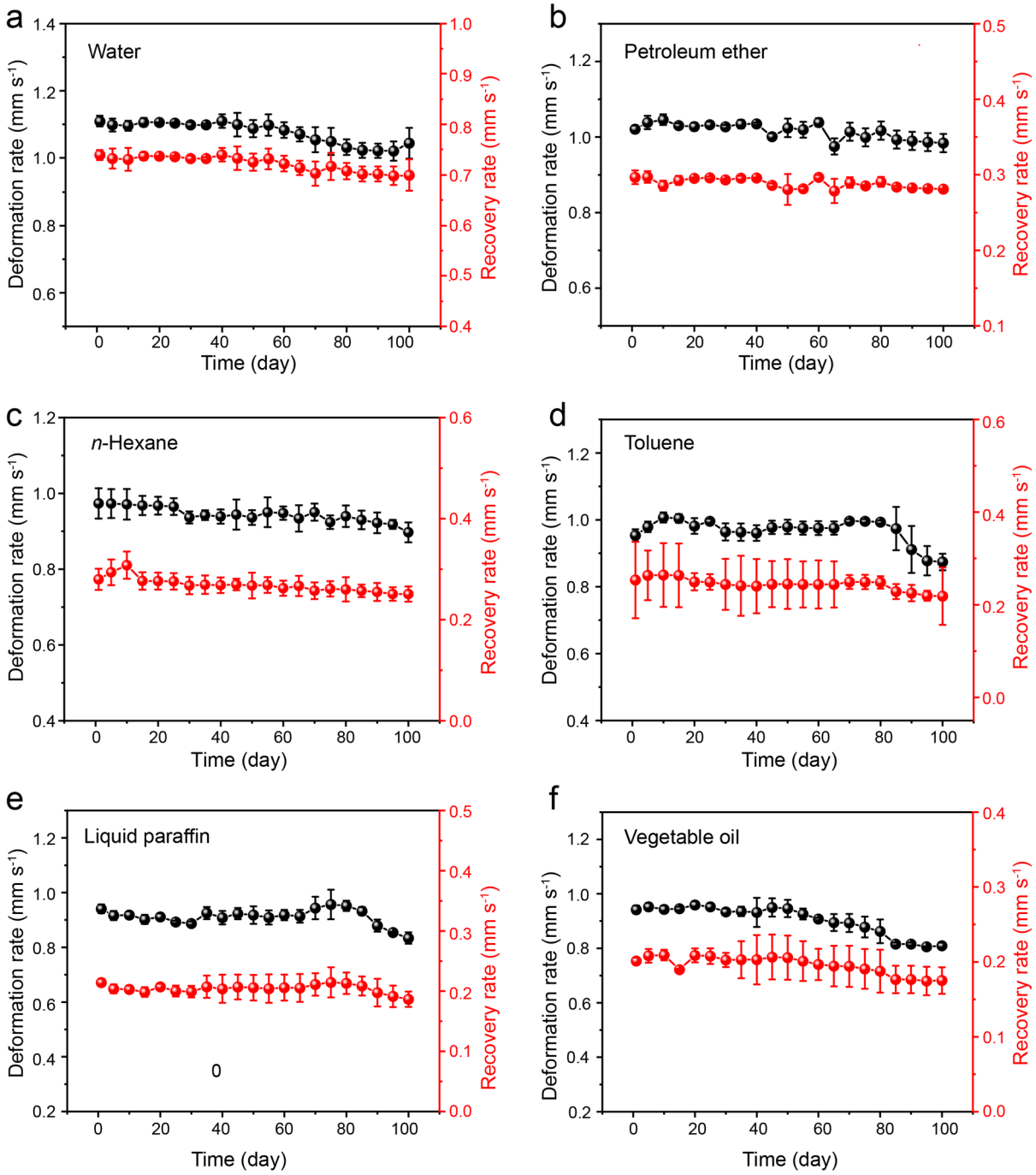

Supplementary Figure 24. Photoresponsive deformation and recovery rates of ASPC hydrogel in 100 days in water (a), *n*-hexane (b), petroleum ether (c), toluene (d), liquid paraffin (e) and vegetable oil (f). Data are presented as mean values ± SD (n = 3).

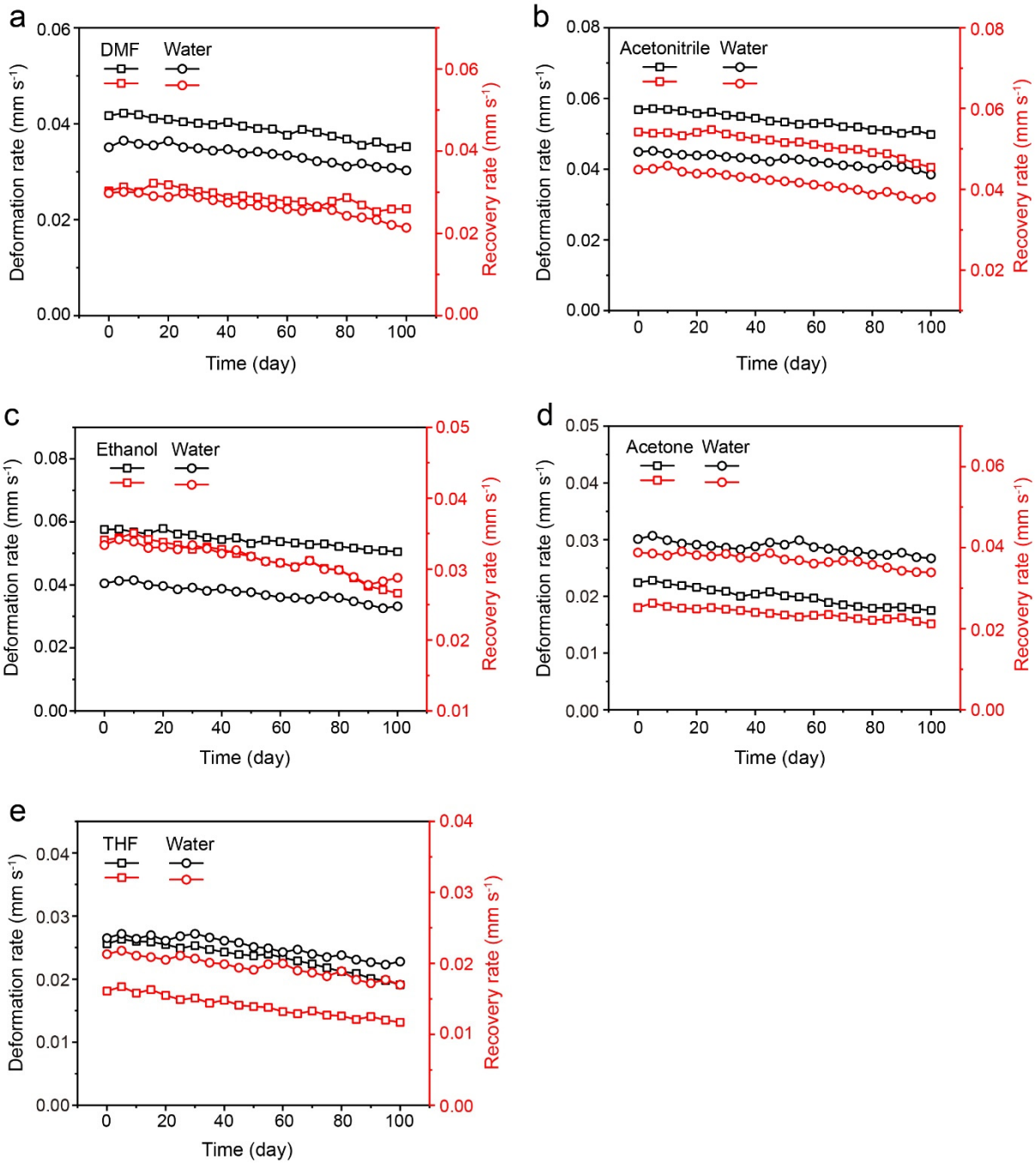

Supplementary Figure 25. Solvent-responsive deformation and recovery rates of ASPC hydrogel in 100 days in DMF (a), acetonitrile (b), ethanol (c), acetone (d) and THF (e).

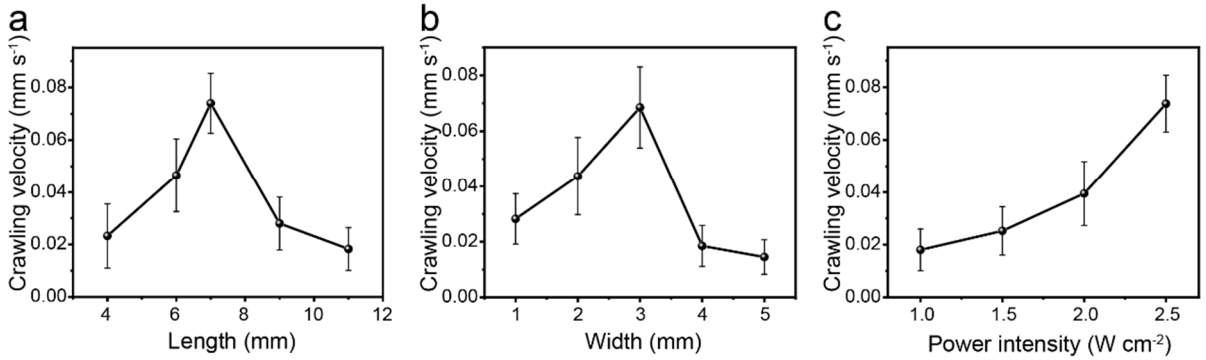

Supplementary Figure 26. Effects of length (a), width (b) and power intensity (c) on the crawling velocity of ASPC hydrogel in water. Data are presented as mean values ± SD (n = 3).

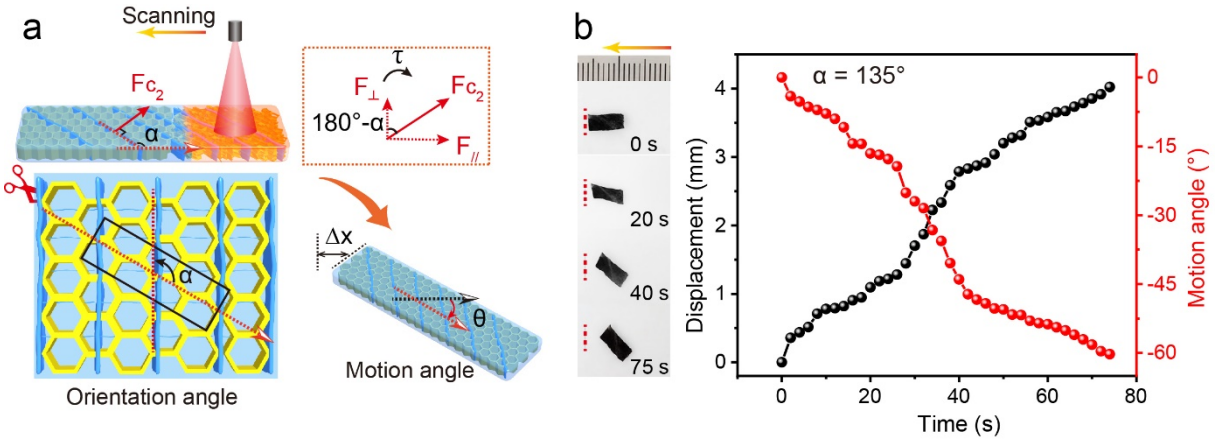

Supplementary Figure 27. (a) Schematic motion programmability and force analysis of hydrogel sheet at 90° < α < 180° when NIR light scanning from right to left. The contraction force Fc_2 acting on the tail was decomposed into a horizontal force $F_{//}$ providing driven force for horizontal movement and a vertical component $F_{\perp}$ driving the motion angle θ. A torque τ was thus generated at the tail. (b) Optical images, time-variant displacements and motion angle of the hydrogel sheets (α = 135°) under cyclic scanning of NIR light (The negative sign indicated a clockwise rotation).

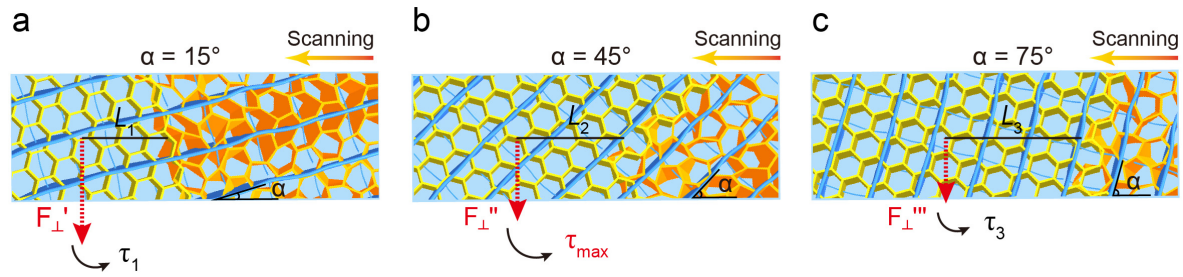

Supplementary Figure 28. Schematic illustration of the force analysis with the α ranging from 0° to 90°. As the α increased, the $F_{\perp}$ decreased as the result of $F_{\perp} = Fc_2 \times \cos\alpha$, while the $F_{//}$ increased as the result of $F_{//} = Fc_2 \times \sin\alpha$. At a larger α, it was faster to achieve energy accumulation threshold that conquered the friction force and triggered the tail to move forward, which produced the head having a shorter irradiated distance. On the other hand, the torque was the product of the force $F_{\perp}$ and force arm L, where the $F_{\perp}$ decreased with the increase of the α ($F_{\perp}' > F_{\perp}'' > F_{\perp}'''$), and the force arm L increased with the increase of the α ($L_1 < L_2 < L_3$). Thus, when α was 45°, the torque driving gel to rotate was the largest, resulting in the largest movement angle.

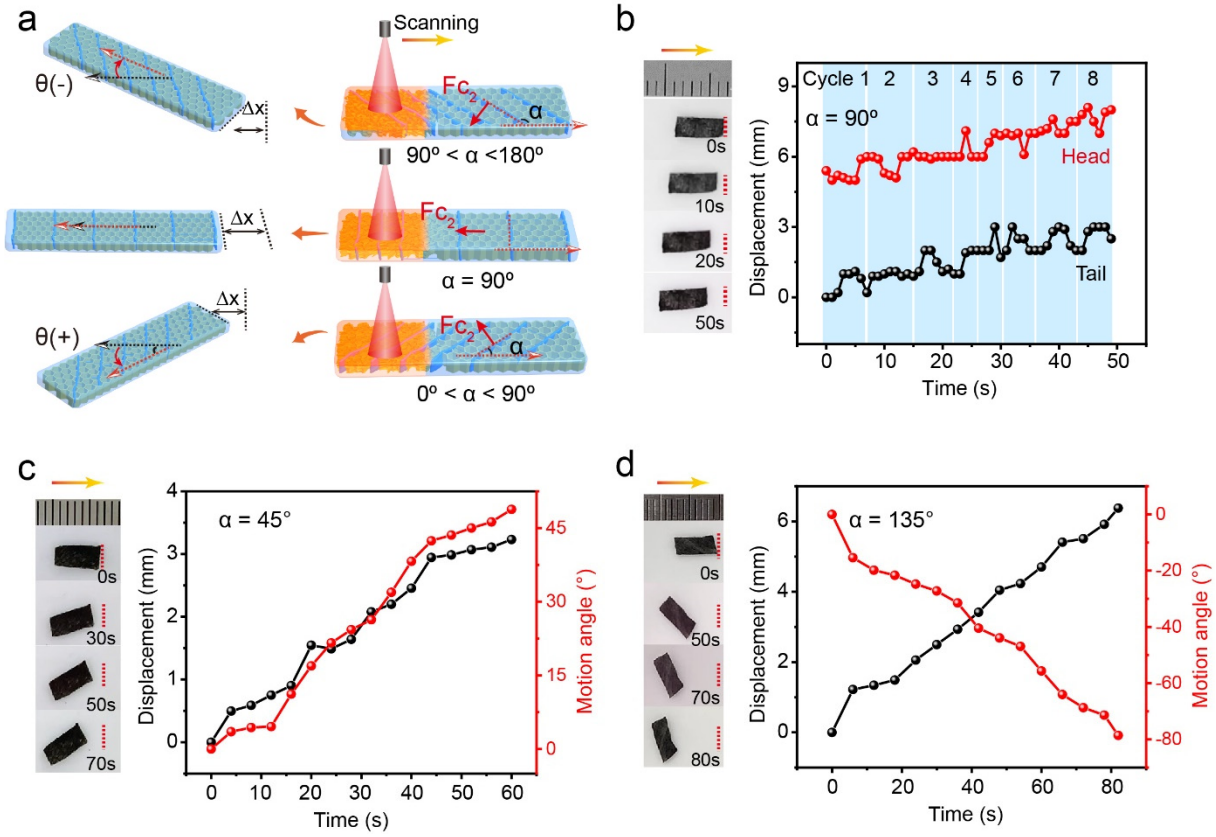

Supplementary Figure 29. The motion trajectories of hydrogel sheets with different α when NIR light scanning from left to right. (a) Schematic diagrams and force analysis of the relationship between α and θ, displacement Δ*x*. At 0° < α < 90°, the hydrogel rotated anticlockwise while crawling. At 90° < α < 180°, the hydrogel rotated clockwise while crawling. At α = 90°, the hydrogel performed linear crawling. (b-d) Optical images and time-variant motion trajectories at different α under cyclic scanning. (b) α = 90°, (c) α = 45° and (d) α = 135°. The light intensity was 2.5 W cm^{-2}.

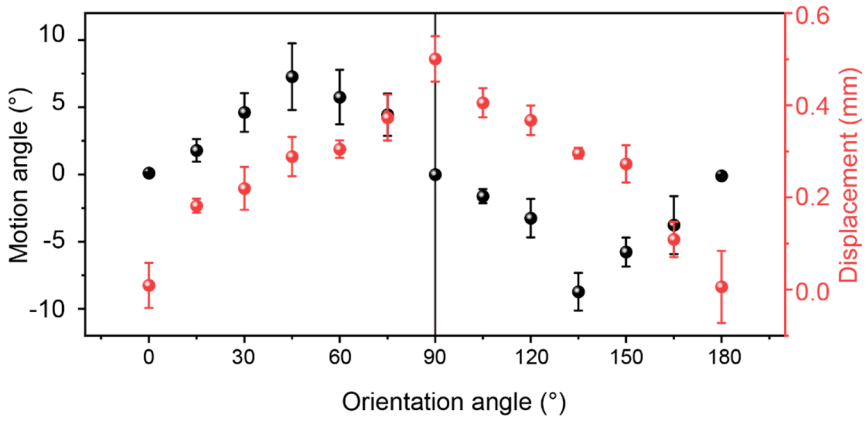

Supplementary Figure 30. The motion angle (black sphere) and displacement (red sphere) were summarized as a function of orientation angle of the hydrogel when NIR light scanning from left to right. The negative signs indicated clockwise movements. Data are presented as mean values ± SD (*n* = 3).

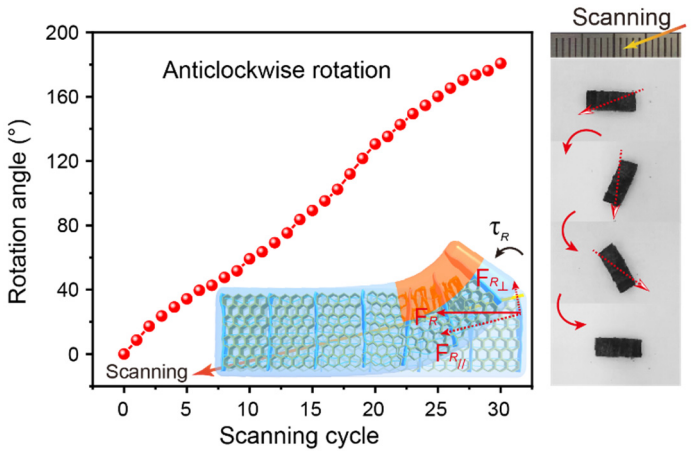

Supplementary Figure 31. Schematic diagram, optical images and rotated angle of the gel (α = 90°) when the light cyclically scanning from the upper right along the diagonal direction. The contraction force of rotation motion F_R was decomposed into component force $F_{R//}$ and $F_{R\perp}$ parallel and perpendicular to the diagonal, respectively. A torque τ was generated to actuate rotational dynamics. The red dashed arrows and red solid arrows indicated the scanning and rotation directions, respectively. Power intensity: 2.5 W cm^{-2}.

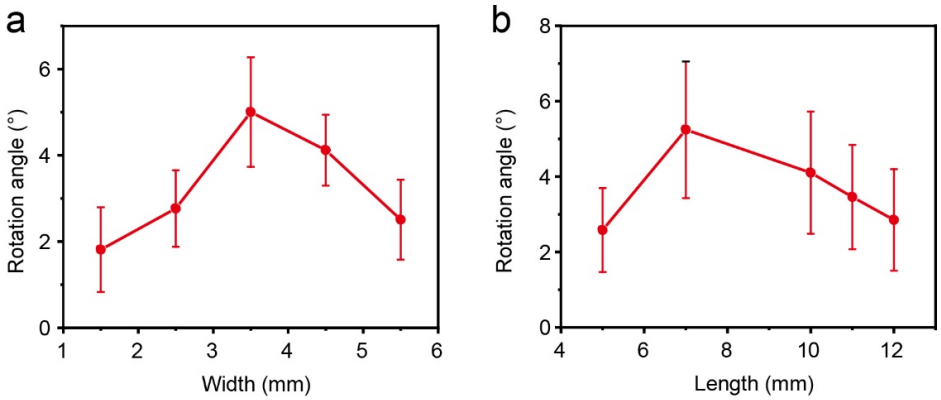

Supplementary Figure 32. Effects of sample width and length on the rotating motions of the hydrogel. Data are presented as mean values ± SD (n = 3).

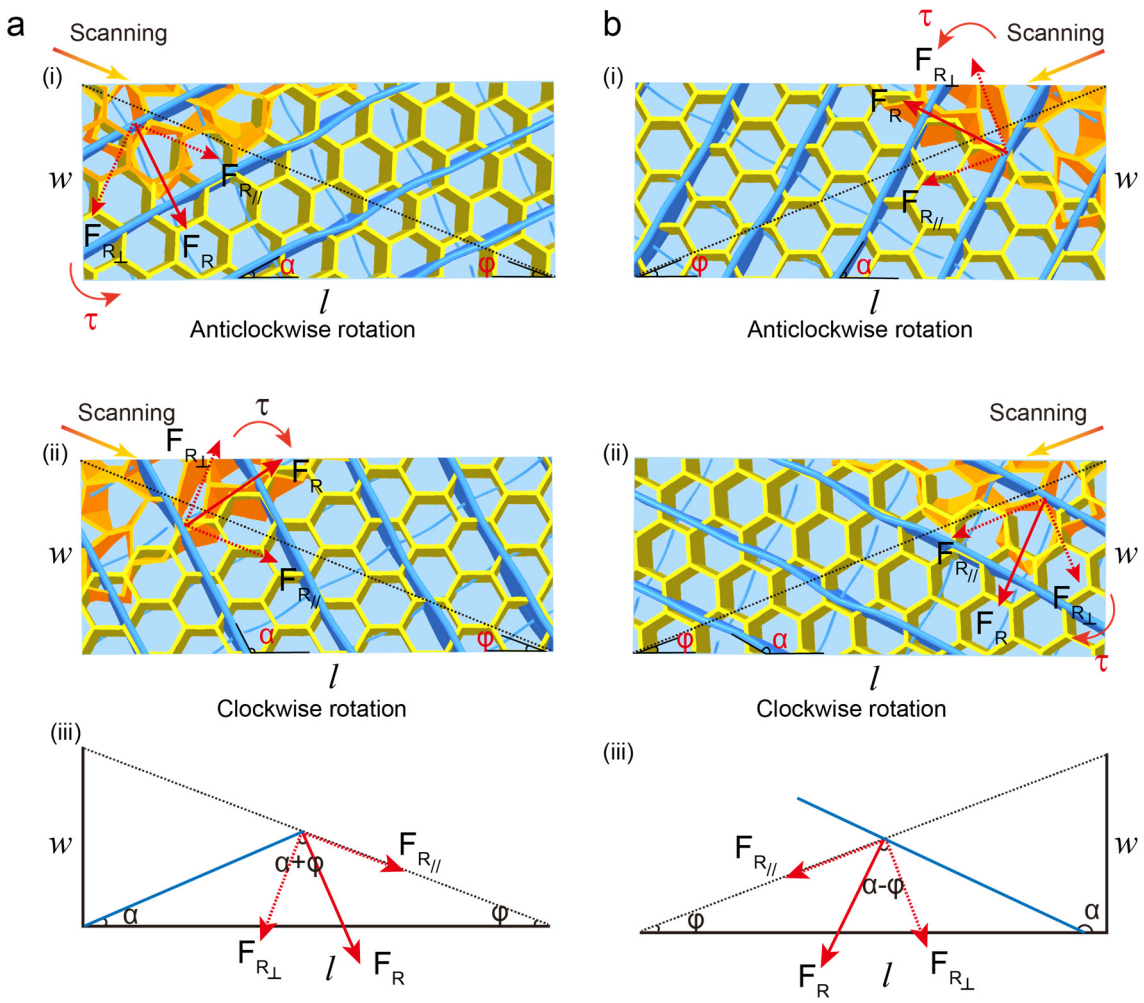

Supplementary Figure 33. Schematic illustrations of the rotation with different α when light scanning diagonally from the upper left corner (a) and the upper right corner (b). Schematic diagrams of (i) anticlockwise and (ii) clockwise rotations. The contraction force F_R was decomposed into component forces $F_{R//}$ and $F_{R\perp}$. A torque τ was generated to actuate rotational dynamics. (iii) Force analysis showing the relationship between α and φ. The angle φ, defined as the angle between diagonal and long axis of the gel, was calculated by the equation: $\tan \varphi = w/l$, where w and l were defined as the width and length of the hydrogel, respectively. Thus, when scanning diagonally from the upper left, the driving force $F_{R\perp}$ was established by the equation: $F_{R\perp} = F_R \times \cos(\alpha + \varphi)$. While the light scanning diagonally from the upper right, the $F_{R\perp}$ was estimated by the equation: $F_{R\perp} = F_R \times \cos(\alpha - \varphi)$.

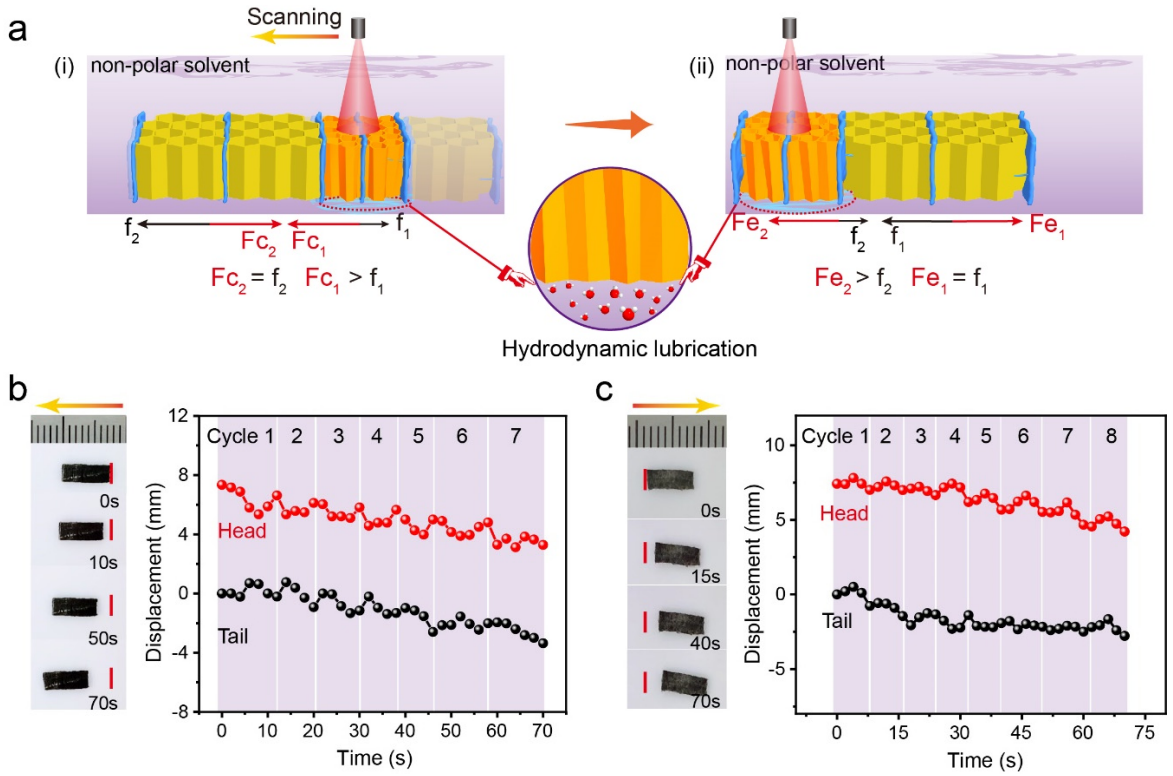

Supplementary Figure 34. Photoinduced crawling of hydrogels (α = 90°) in non-polar solvents. (a) Schematic illustration of the photo-driven motion in non-polar solvents. When the light irradiated the gel head, the water released from the hydrophilic-hydrophobic conversion of the polymer surrounded the bottom of the gel, forming a hydrodynamic lubrication layer between the gel and the substrate, so that the contraction force Fc_1 overcame the friction resistance f_1, causing the head to move to the tail (i). When light irradiated the tail of gel, the lubrication of the tail led to the reduction of friction. Thus, the expansion force Fe_2 generated by the rapid water absorption of the head overcame f_2, causing the head to move backward (ii). Optical images and time-variant displacements of the head and tail in *n*-hexane under cyclic scanning of NIR light from right to left (b) and from left to right (c). The negative signs indicated that the displacement direction was consistent with the scanning direction. The light intensity was 2.0 W cm^{-2}.

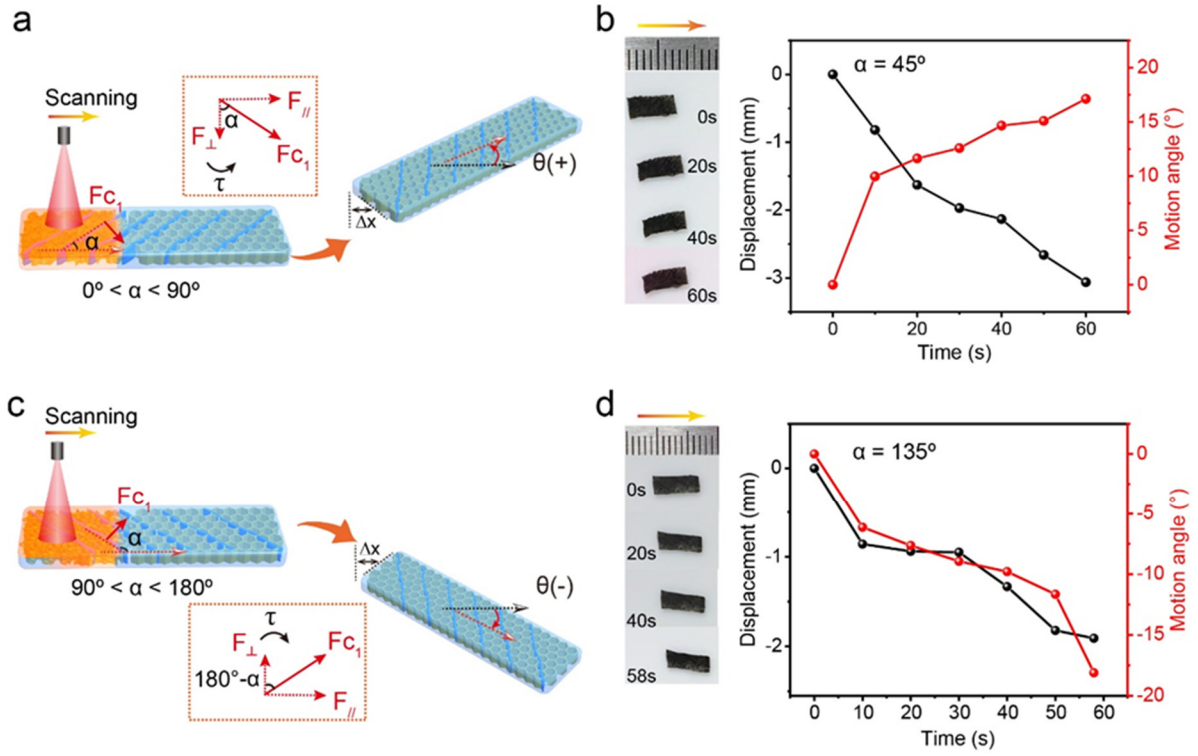

Supplementary Figure 35. The motion programmability of hydrogel at different α in *n*-hexane. Schematic diagram and force analysis of the motion trajectories of hydrogel sheets at 0° < α < 90° (a) and 90° < α < 180° (c). Optical images and time-variant displacements under cyclic scanning at α = 45° (b) and α = 135° (d). The negative sign of displacement indicated the motion direction consistent with the scanning direction, and the negative sign of motion angle indicated clockwise rotation.

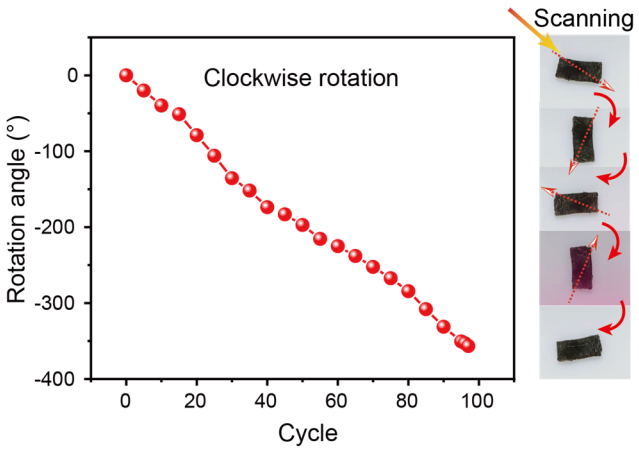

Supplementary Figure 36. The clockwise rotation of hydrogel (α = 90°) in *n*-hexane. Optical images and rotated angle of the hydrogel under cyclic NIR scanning. When NIR light scanning diagonally from the top-left corner, the gel rotated clockwise by 356°. The light intensity was 2.0 W cm^{-2}.

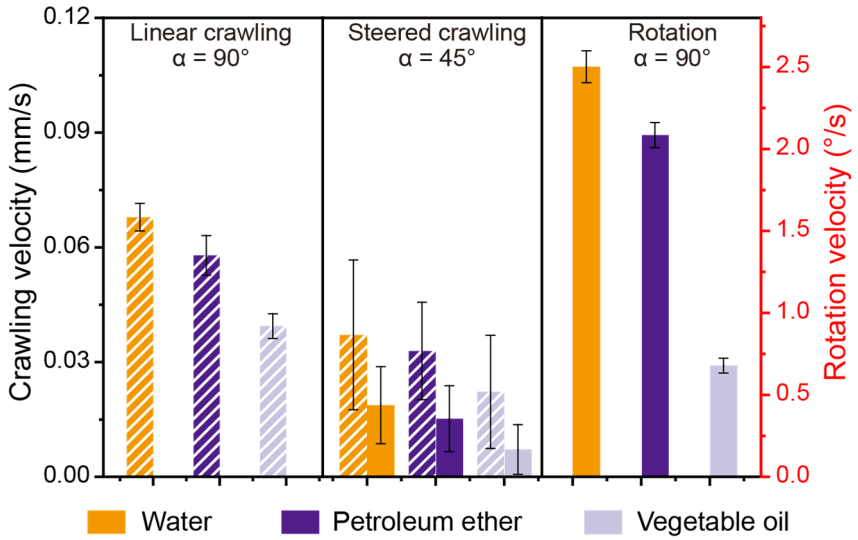

Supplementary Figure 37. Summary of linear crawling, steered crawling and rotated velocity in solvents of water, petroleum ether and vegetable oil. The striped and solid columns indicated crawling velocity and rotation velocity, respectively. Data are presented as mean values ± SD (n = 3).

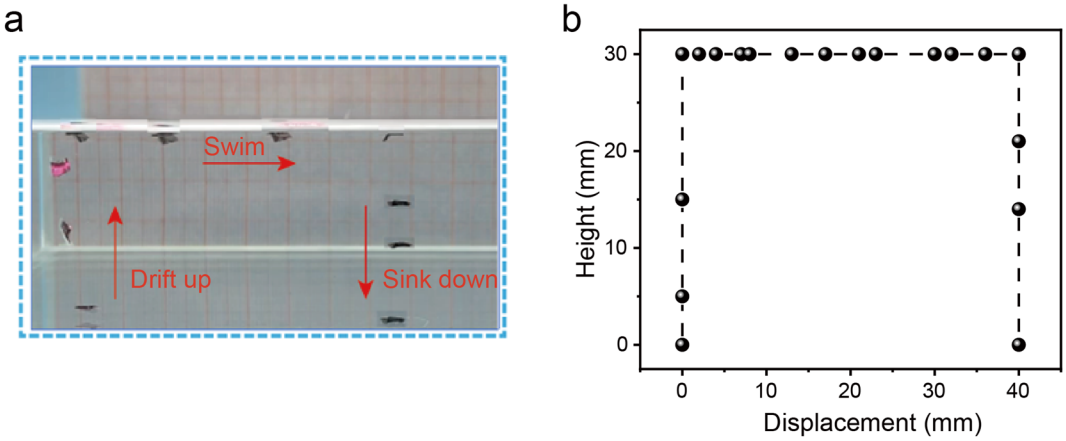

Supplementary Figure 38. Optical images (a) and trajectory (b) of the swimmer during 3D locomotion process. Light intensity: 2.5 W cm^{-2}.

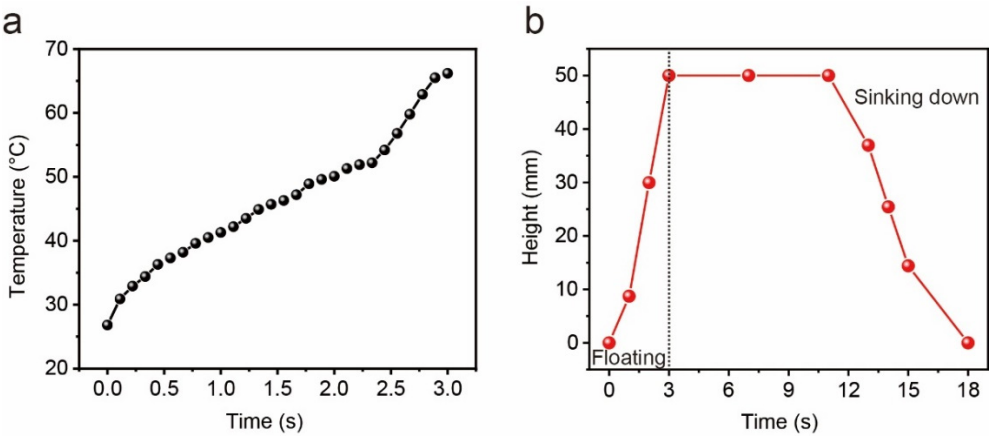

Supplementary Figure 39. (a) Time-dependent temperature of hydrogel in the floating by NIR irradiation. (b) Time-dependent height of hydrogel induced by photothermal buoyancy flow. Light intensity: 2.5 W cm^{-2}.

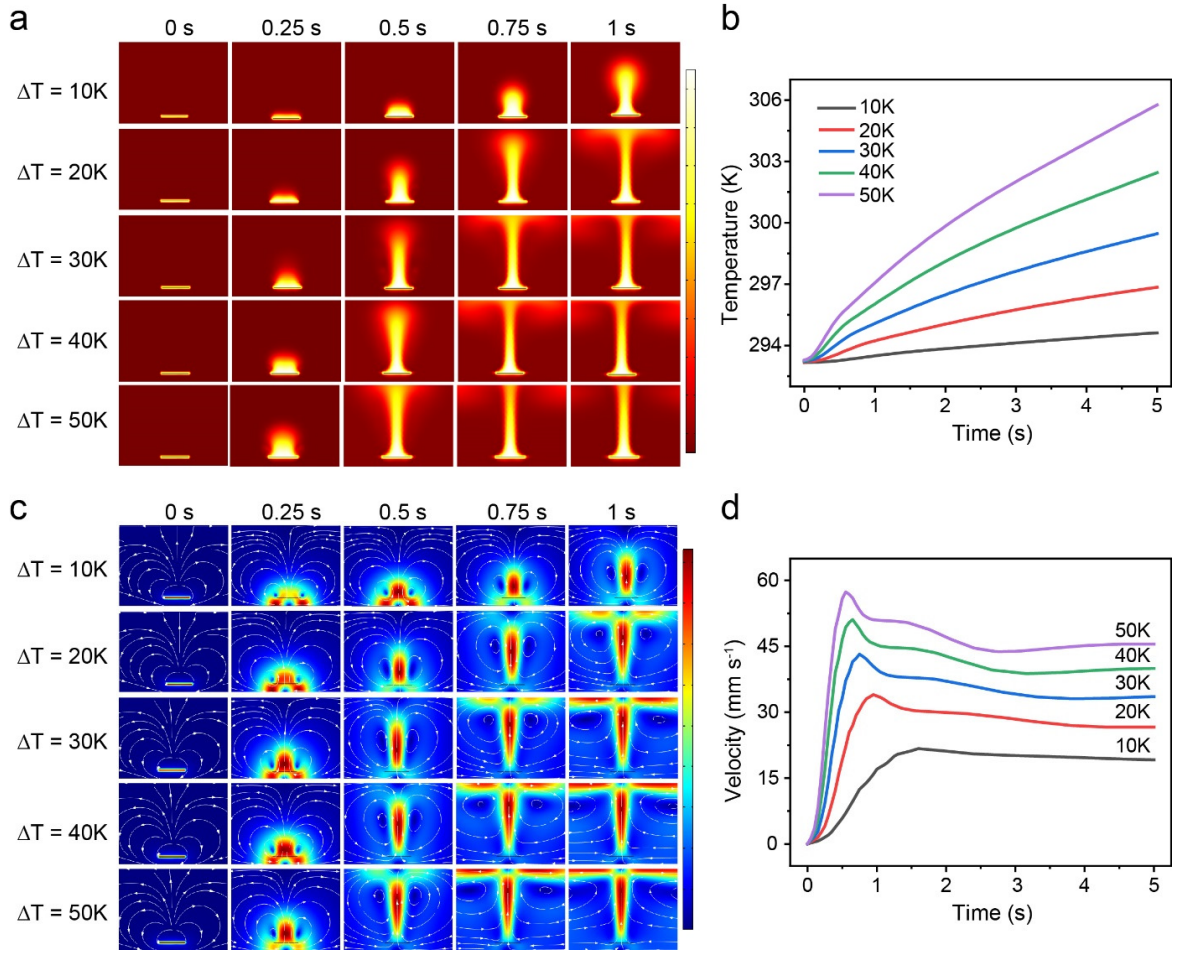

Supplementary Figure 40. The simulation results of temperature distribution (a) and floating velocity distribution (c) under temperature difference (ΔT) of 10 K, 20 K, 30 K, 40 K and 50 K. (b) The average temperature of the whole liquid under different ΔT. (d) Maximum flow velocity at different times under different ΔT.

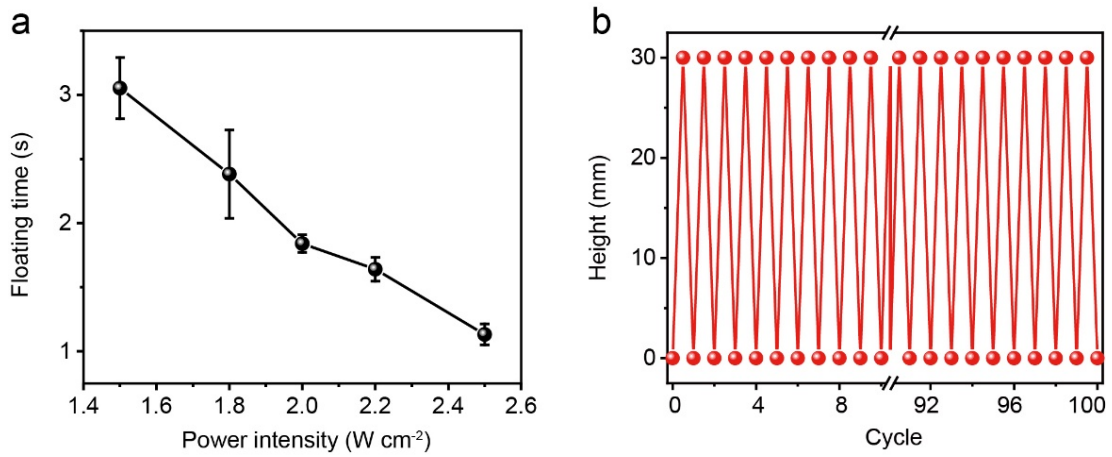

Supplementary Figure 41. (a) Floating time of hydrogel under different laser intensities. As the laser power increases, the colloidal collective would absorb more light energy, converting it into more heat and thus inducing a greater rate of buoyant flow. The height of the ethanol solvent was 30 mm. Data are presented as mean values ± SD (n = 3). (b) Plots of reversible floating-sinking cycle of hydrogel upon exposure to NIR light in ethanol at a depth of 30 mm (100 cycles without obvious fatigue). The light intensity was 2.5 W cm^{-2}.

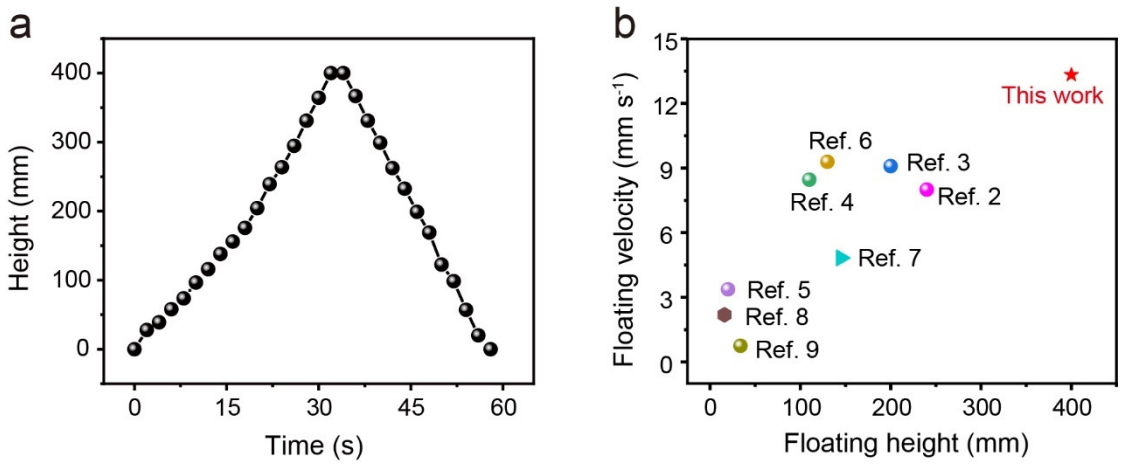

Supplementary Figure 42. (a) Time-dependent height of hydrogel floating in ethanol with a depth of 400 mm. (b) Floating height versus corresponding velocity of swimmer in comparison with previous reports. Spheres, hexagons and triangles represented hydrogel-based[2-7], dielectric elastomer-based[8] and liquid crystal gel-based[9] swimmers, respectively.

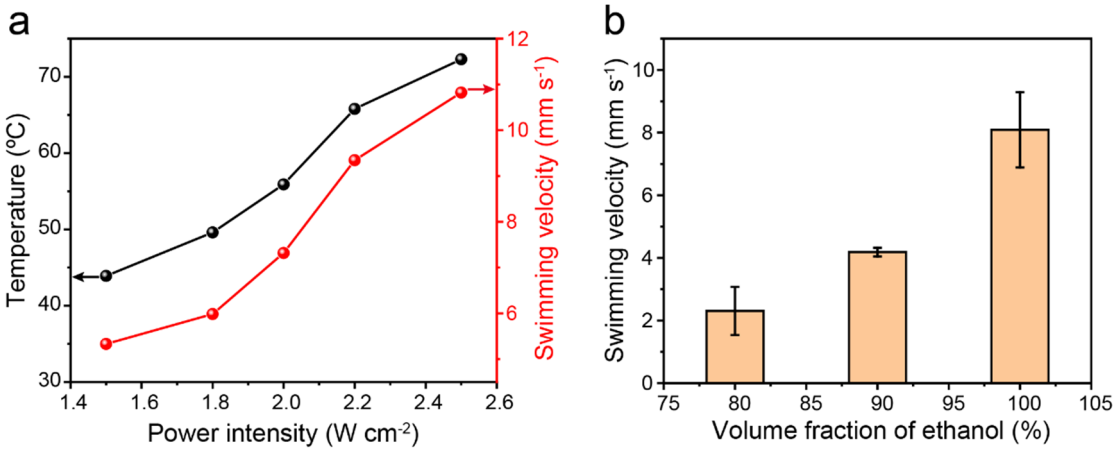

Supplementary Figure 43. (a) The temperature and swimming velocity at different power intensities. (b) The swimming velocity at different volume fractions of ethanol. Data are presented as mean values ± SD (n = 3).

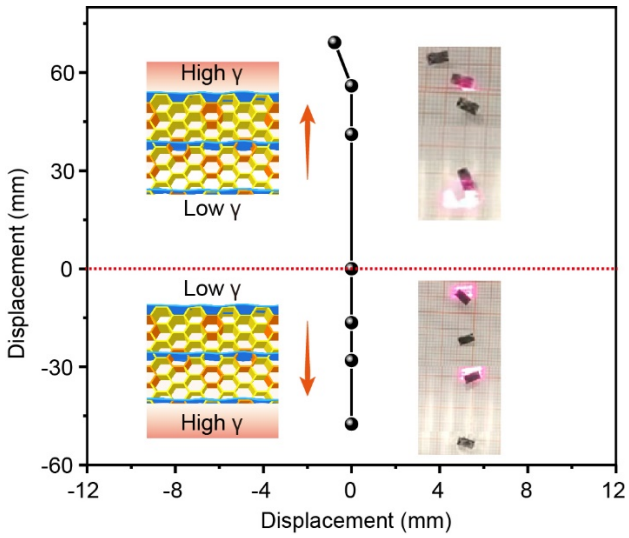

Supplementary Figure 44. Schematic illustration and superimposed photographs of linear swimming. At α = 0°, the direction of the contraction force was consistent with the direction of the Marangoni propulsion force, resulting in a linear swimming motion. The hydrogel swam upward when the bottom irradiated, and swam downward when the top irradiated. The motion directions were indicated by red arrows and the light intensity was 2.5 W cm^{-2}.

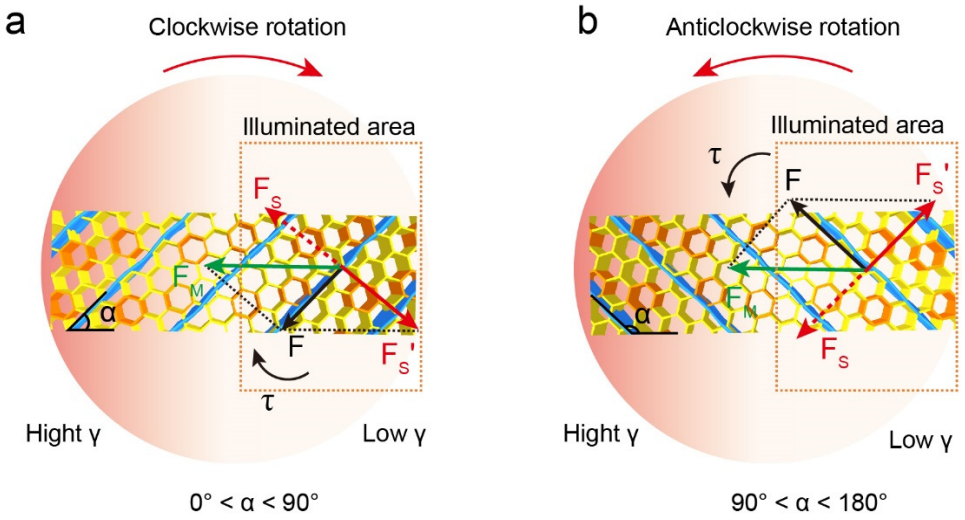

Supplementary Figure 45. Mechanisms of the swimming with programmable directionality. Under irradiation, surface tension gradient was generated between the gel and surrounding liquid, resulting in a propulsion force F_M along the surface tension gradient. The contraction of the irradiated network generated a pair of contraction force Fs and Fs' perpendicular to the layer. The resultant force F between F_M and Fs' led to a torque τ that tended to rotate the hydrogel, where the τ direction depended on the magnitude of α. The gel swam clockwise when 0° < α < 90° (a) and anticlockwise when 90° < α < 180° (b). The orange dashed box represented the irradiation area, where the surface tension decreased with the increase in temperature.

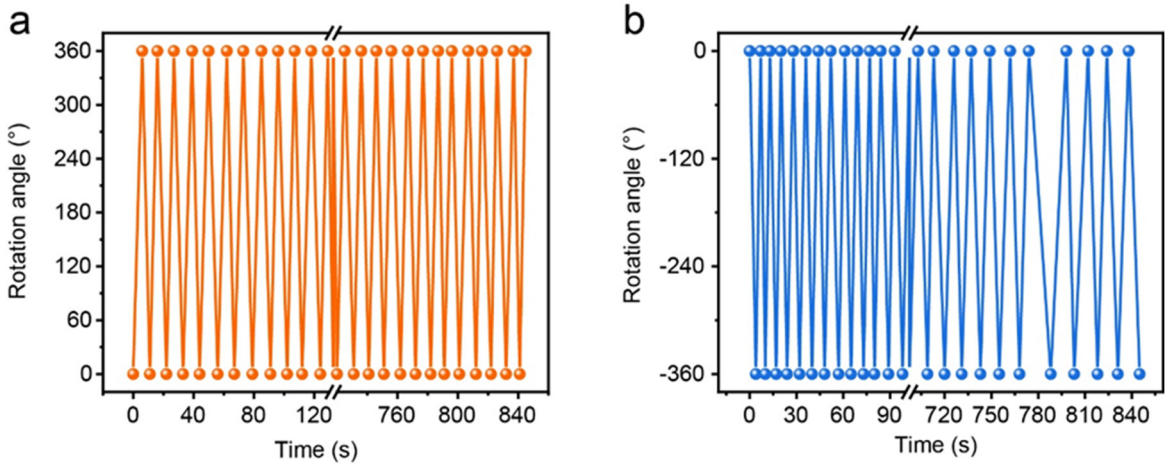

Supplementary Figure 46. Stable rotation under continuous irradiation in ethanol. (a) The hydrogel (α = 135°) rotated anticlockwise for 845 s. (b) The hydrogel (α = 45°) rotated clockwise for 845 s. The light intensity was 2.0 W cm^{-2}.

Supplementary References

1. Yang, C. et al. Silver nanowires: From scalable synthesis to recyclable foldable electronics. *Adv. Mater.* **23,** 3052-3056 (2011).
2. Pan, D. et al. Transparent light-driven hydrogel actuator based on photothermal marangoni effect and buoyancy flow for three-dimensional motion. *Adv. Funct. Mater.* **31,** 2009386 (2021).
3. Hou, G. et al. Self-regulated underwater phototaxis of a photoresponsive hydrogel-based phototactic vehicle. *Nat. Nanotechnol.* **19,** 77-84 (2024).
4. Wang, L. et al. A bioinspired swimming and walking hydrogel driven by light-controlled local density. *Adv. Sci.* **2,** 1500084 (2015).
5. Yin, C. et al. Visible light-driven jellyfish-like miniature swimming soft robot. *ACS Appl. Mater. Interfaces* **13,** 47147-47154 (2021).
6. Du, X. et al. Reconfiguration, camouflage, and color-shifting for bioinspired adaptive hydrogel-based millirobots. *Adv. Funct. Mater.* **30,** 1909202 (2020).
7. Zong, L. et al. Activation of actuating hydrogels with WS_2 nanosheets for biomimetic cellular structures and steerable prompt deformation. *ACS Appl. Mater. Interfaces* **9,** 32280-32289 (2017).
8. Wang, Y. et al. Bio-inspired transparent soft jellyfish robot. *Soft Robot* **10,** 590-600 (2023).
9. Shahsavan, H. et al. Bioinspired underwater locomotion of light-driven liquid crystal gels. *Proc. Natl. Acad. Sci.* **117,** 201917952 (2020).